Revised MS# nn-2014-06387w

Atomic Layer-by-Layer Deposition of Pt on Pd Octahedra for Enhanced Catalysts toward the Oxygen Reduction Reaction

Jinho Park,[†,#] Lei Zhang,[‡,#] Sang-Il Choi,[‡] Luke T. Roling,[§] Ning Lu,[‖] Jeffrey A. Herron,[§] Shuifen Xie,[‡] Jinguo Wang,[‖] Moon J. Kim,[‖] Manos Mavrikakis,[§] and Younan Xia*,[†,‡]

[†]School of Chemistry and Biochemistry, Georgia Institute of Technology, Atlanta, Georgia 30332, Unites States

[‡]The Wallace H. Coulter Department of Biomedical Engineering, Georgia Institute of Technology and Emory University, Atlanta, Georgia 30332, Unites States

[§]Department of Chemical and Biological Engineering, University of Wisconsin-Madison, Madison, Wisconsin 53706, United States

[‖]Department of Materials Science and Engineering, University of Texas at Dallas, Richardson, Texas 75080, United States

[#]These two authors contributed equally to this work.

*Corresponding author: younan.xia@bme.gatech.edu

ABSTRACT We systematically evaluated two different approaches to the syntheses of Pd@Pt$_{n\mathrm{L}}$ (n=2−5) core-shell octahedra. We initially prepared the core-shell octahedra using a polyol-based route by titrating a Pt(IV) precursor into the growth solution containing Pd octahedral seeds at 200 ^{o}C through the use of a syringe pump. The number of Pt atomic layers could be precisely controlled from two to five by increasing the volume of the precursor solution while fixing the amount of seeds. We then demonstrated the synthesis of Pd@Pt$_{n\mathrm{L}}$ octahedra using a water-based route at 95 ^{o}C through the one-shot injection of a Pt(II) precursor. Due to the large difference in reaction temperature, the Pd@Pt$_{n\mathrm{L}}$ octahedra obtained *via* the water-based route showed sharper corners than their counterparts obtained through the polyol-based route. When compared to a commercial Pt/C catalyst based upon 3.2-nm Pt particles, the Pd@Pt$_{n\mathrm{L}}$ octahedra prepared using both methods showed similar remarkable enhancement in terms of activity (both specific and mass) and durability toward the oxygen reduction reaction. Calculations based upon periodic, self-consistent density functional theory suggested that the enhancement in specific activity for the Pd@Pt$_{n\mathrm{L}}$ octahedra could be attributed to the destabilization of OH on their Pt$_{n\mathrm{L}}$*/Pd(111) surface relative to the {111} and {100} facets exposed on the surface of Pt/C. The destabilization of OH facilitates its hydrogenation, which was found to be the rate-limiting step of the oxygen reduction reaction on all these surfaces.

KEYWORDS platinum-based electrocatalysts, core-shell nanocrystals, octahedra, oxygen reduction reaction, density functional theory

TOC

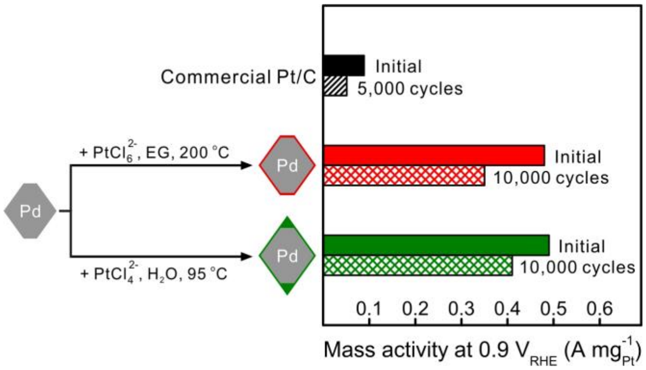
Commercial Pt/C
Initial
5,000 cycles
+ PtCl$_6^{2-}$, EG, 200 °C
+ PtCl$_4^{2-}$, H$_2$O, 95 °C
Pd
Pd
Pd
Initial
10,000 cycles
Initial
10,000 cycles
0.1 0.2 0.3 0.4 0.5 0.6
Mass activity at 0.9 V$_{RHE}$ (A mg$_{Pt}^{-1}$)

Platinum is a key component of the catalyst used for the oxygen reduction reaction (ORR) in a proton-exchange membrane fuel cell (PEMFC).[1−5] Despite its superb performance in catalyzing ORR, its high cost and low abundance in the earth's crust have created a major barrier for the large-scale commercialization of PEMFCs as a clean-energy technology.[6,7] According to a 2012 report from the Department of Energy, the Pt loading in a PEMFC has to be reduced by at least four folds in order to meet the cost requirement for profitable marketing.[7]

For several decades, people have been actively searching for methods capable of improving the mass activity (per unit mass of Pt, A mg_{Pt}^{-1}) and durability of a Pt-based catalyst and thereby reducing the Pt loading. In general, the activity and durability of a catalyst can be improved by engineering the size, shape, structure, and composition of the nanoparticles involved.[8−19] To this end, Pt-based bimetallic nanoparticles have been demonstrated with remarkable performance in catalyzing ORR.[12−19] The bimetallic nanoparticles have been synthesized with a number of different structures, including alloy,[13−15] dendrite,[16] and core-shell.[17−19] Among them, Pt-Ni alloy octahedra represented the most successful development in recent years due to their record-setting activity, but their poor durability arising from the dissolution of Ni still needs to be addressed.[14] Alternatively, deposition of a few atomic layers of Pt on the surface of facet-controlled nanocrystals made of another metal such as Pd also offers an attractive strategy for maximizing the activity in terms of Pt mass.[20] This strategy can reduce the materials cost of a catalyst by replacing the Pt in the core with a much less expensive metal.[12] It can also retain the dispersion of Pt atoms while increasing the durability of a catalyst by switching to nanoparticles with larger sizes. In addition, the inclusion of a different metal can alter the electronic structure of Pt through ligand and strain effects, leading to potential enhancement in specific activity.[12, 21−26]

In a recent study, we successfully synthesized $Pd@Pt_{nL}$ core-shell nanocubes *via* conformal, epitaxial deposition of Pt on Pd nanocubes, where the number (n) of Pt atomic layers could be precisely controlled from a monolayer to multiple layers.[27] When compared to a commercial Pt/C catalyst, the $Pd@Pt_{nL}$ nanocubes showed enhancement in both mass activity (by three folds) and durability toward ORR. Because the Pt atoms were well-dispersed on the surfaces of the Pd cores as ultrathin shells, the $Pd@Pt_{nL}$ nanocubes exhibited higher electrochemical surface areas (ECSAs) than the Pt/C reference despite their marked difference in particle size (20 nm *vs.* 3.2 nm). The high dispersion of Pt atoms made a critical contribution to the enhancement in mass activity. While this prior work demonstrated the feasibility to improve the catalytic performance, the cubic shape is not an optimal choice for the development of effective ORR catalysts. For ORR catalysts based upon Pt, previous studies have established that the (111) surface has a specific activity of at least two-fold higher than that of the (100) surface.[28−30] As a result, there exists a strong incentive to epitaxially deposit Pt atoms as atomic overlayers on Pd octahedra to achieve a higher electrocatalytic activity than what was previously reported for the cubic system.

The synthesis of Pd@Pt core-shell nanocrystals *via* seeded growth typically suffers from an island growth mode or self-nucleation for the Pt atoms because the bond energy of Pt-Pt (307 kJ mol^{-1}) is much higher than that of Pd-Pt (191 kJ mol^{-1}).[16] It has been reported that monolayers or sub-monolayers of Pt could be deposited on Pd nanocrystals using an electrochemical approach by taking advantage of the galvanic replacement reaction between the underpotentially deposited monolayers of Cu and a Pt(II) precursor.[31,32] The capability of this method will be limited in terms of scale-up production due to the involvement of electrodes in the deposition process. In a recent study, we demonstrated that Pt atoms could be deposited as uniform, conformal, ultrathin overlayers on Pd nanocubes *via* a solution-phase process that involves the use of a polyol such as ethylene glycol (EG).[27,33] At a relatively high reaction temperature of 200 ^{o}C, the deposited Pt atoms could be promoted to diffuse across the Pd surface to generate Pt shells in a layer-by-layer fashion. In principle, this protocol could be extended to generate conformal shells of Pt on Pd octahedra. However, because Pd(111) has a much lower surface free energy than Pd(100), it is anticipated that the original deposition protocol would be troubled by the complications caused by the self-nucleation of Pt atoms.[34]

Here we compare two different protocols based upon polyol and aqueous solutions for the epitaxial, conformal deposition of Pt on Pd octahedra to generate Pd@Pt_{nL} octahedra (n=2−5). For the polyol-based system, we simply used the protocol developed for Pd@Pt_{nL} nanocubes[27] with a minor modification to address the self-nucleation issue by decreasing the concentration of the Pt(IV) precursor. When switched to an aqueous system, we could achieve similar conformal deposition of Pt on Pd octahedra at a much lower temperature (95 ^{o}C *vs.* 200 ^{o}C), which should be more attractive as a cost-saving and environment-friendly process.[35] To avoid self-nucleation for the newly formed Pt atoms in an aqueous system, we employed a mild reducing agent to slow down the reduction of a Pt(II) precursor. Prior to the synthesis of Pd@Pt_{nL} octahedra, we also performed periodic, self-consistent density functional theory (DFT) calculations using extended surface models of the nanocrystal terraces. The calculation results confirmed that the Pd@Pt_{nL}

(n=2−5) octahedra indeed had higher specific activity than both the commercial Pt/C catalyst and Pd@Pt$_{n\mathrm{L}}$ (n=2−5) nanocubes,[27] owing to the increased destabilization of OH on the surfaces of Pd@Pt$_{n\mathrm{L}}$ octahedra. Experimentally, we demonstrated that both the specific and mass activities of the Pd@Pt$_{n\mathrm{L}}$ octahedra were greatly enhanced relative to a commercial Pt/C. The Pd@Pt$_{n\mathrm{L}}$ octahedra also exhibited substantial improvement in durability toward ORR thanks to the use of catalytic particles with a greatly enlarged size (20 nm *vs.* 3.2 nm).

RESULTS AND DISCUSSION

Comparison of the ORR activities of Pd@Pt$_{n\mathrm{L}}$ (n=2−5) octahedra by DFT calculation. Before conducting the synthesis, we compared the ORR activities of Pd@Pt$_{n\mathrm{L}}$ (n=2−5) octahedra by computing the energetics of oxygen reduction on model surfaces with periodic, self-consistent DFT (see the Supporting Information for details). Specifically, the Pd@Pt$_{n\mathrm{L}}$ octahedra were modeled as Pt$_{n\mathrm{L}}$*/Pd(111) extended surfaces whereas Pt solid octahedra were represented by the Pt(111) surface. Due to the compositional instability associated with the Pt$_{1\mathrm{L}}$*/Pd(111) surface (Figure S1), we decided not to consider Pd@Pt$_{1\mathrm{L}}$ octahedra in the present work. We obtained the reaction thermochemistry (Table S1) at 0.9 V$_{\mathrm{RHE}}$ (with reference to the reversible hydrogen electrode, RHE) from the computed binding energies (Table S2).[36] Based upon the reaction thermochemistry,[37] it can be concluded that the rate-limiting step is $OH^* + H^+ + e^- \rightarrow H_2O$ for all these systems. We also noted that the reaction energy for this step is determined by the binding energy of OH, and the reaction endothermicity increases with increasing the absolute binding energy of OH. Our analysis indicates that the this step becomes more facilitated on Pt$_{n\mathrm{L}}$*/Pd(111) (n=2−5) than Pt(111). In addition, prior theoretical calculations and experimental measurements indicate that the specific ORR activity of Pt(111) is higher than that of Pt(100) in the presence of a non-adsorbing electrolyte such as $HClO_4$.[28−30] As shown in Figure 1, the calculation results clearly indicated that each of the Pt$_{n\mathrm{L}}$*/Pd(111) (n=2−5) surfaces had a higher specific activity than pure Pt(111). As a result, the Pd@Pt$_{n\mathrm{L}}$ (n=2−5) octahedra were anticipated to exhibit enhanced specific ORR activity relative to Pt octahedra. We note that the relative ordering of activities for the 2L, 3L, and 4L model surfaces follow the trend for the d_{z^2}-band center, which, in turn, determines the binding energy of OH on these surfaces (Table S3). It is nontrivial to deconvolute the lattice strain effect from the ligand effect on the binding energy of OH; however, our results suggest that both effects are important in enhancing the ORR specific activity (Table

S2). The minor lattice compression imposed by the deposition of Pt atoms on a lattice of slightly smaller Pd atoms causes destabilization of OH, while electronic interactions between the Pd substrate and the Pt overlayers can modulate the OH binding energy depending on the number of Pt layers. Since the Pt atoms of a core-shell nanocrystal are much better dispersed than those of a Pt solid octahedron with a similar size, all the $Pd@Pt_{nL}$ (n=2−5) octahedra are supposed to exhibit greatly enhanced mass activity in terms of Pt. Furthermore, each $Pd@Pt_{nL}$ nanocrystal should be less expensive than a solid Pt octahedron with a similar size because the current price of Pd is only half of that of Pt. Taken together, there is a strong incentive to synthesize $Pd@Pt_{nL}$ (n=2−5) octahedra and then explore them as a new class of ORR catalysts.

Comparison of two different protocols for the syntheses of $Pd@Pt_{nL}$ octahedra. Figure 2 shows a schematic illustration of the polyol- and water-based protocols for the syntheses of $Pd@Pt_{nL}$ octahedra. Both systems involved the use of Pd octahedra with slight truncation at corner sites as the seeds (see Figure S2 for typical TEM images). In general, Pd is a good substrate for the epitaxial overgrowth of Pt due to their close match in lattice constant. However, due to a lower surface free energy for Pd(111) relative to Pd(100), it has been hard to completely prevent the newly formed Pt atoms from self-nucleation in an attempt to obtain $Pd@Pt_{nL}$ octahedra in high purity. This problem was found to be particularly serious when we were trying to directly use the polyol-based protocol developed for coating Pt on Pd cubic seeds (Figure S3).[27] This issue could be addressed by reducing the concentration of the Na_2PtCl_6 precursor solution. Due to the use of a relatively high temperature at 200 °C, the $Pd@Pt_{nL}$ octahedra tended to be truncated at the corner sites, just like the original Pd octahedral seeds. The presence of Pt{100} facets at the corner sites is expected to compromise the specific ORR activity of the resultant nanocrystals.

In addition to the use of polyol and a relatively high temperature, we also tried a water-based protocol conducted at a much lower temperature for the synthesis of $Pd@Pt_{nL}$ octahedra. Unlike the synthesis of $Pd@Pt_{nL}$ cubes, which has to be carried out in a polyol at 200 °C, we could achieve conformal deposition of Pt on Pd octahedra in water at a temperature as low as 95 °C. Related to the issue of temperature, we used DFT calculations (see the Supporting Information for details) to compare the activation energy barriers for a Pt adatom to diffuse across Pd(111) and Pd(100) surfaces, respectively. It was found that the barrier was only 0.16 eV on Pd(111) while it was increased by almost seven folds to 1.06 eV on Pd(100). This result confirms the feasibility to achieve a uniform, conformal coating of Pt on a Pd octahedron *via* surface diffusion at a much lower temperature as compared to the coating of a Pd cube. In the case of water-based synthesis, we also observed sharpening of corners for the core-shell nanocrystals due to the use of a much lower temperature relative to the polyol-based system. To address the self-nucleation issue in the water-based system, we used a weak reducing agent such as citric acid (CA) to slow down the reduction of a Pt(II) precursor. By doing so, we could even introduce the Pt(II) precursor in one-shot and still obtained Pd@Pt$_{n\mathrm{L}}$ octahedra with a purity approaching 100%. The introduction of precursor in one-shot represents another advantage for the possible extension of this protocol to a droplet-based system for the purpose of continuous, scalable production.[38]

Synthesis of Pd@Pt$_{n\mathrm{L}}$ octahedra using the polyol-based protocol. For the polyol-based system, we used Pd octahedra with slight truncation at corner sites as the seeds (Figure S2A). The synthesis was conducted by slowly injecting the Na_2PtCl_6 precursor solution into EG containing PVP, KBr, ascorbic acid (AA), and the Pd seeds at 200 °C under magnetic stirring. Similar to our previous work,[27] the thickness of the Pt shells could be readily controlled with atomic precision by changing the amount of Pt(IV) precursor added into the growth solution. Figure 3 shows TEM images of the Pd@Pt$_{n\mathrm{L}}$ octahedra obtained using the polyol-based protocol. The number of Pt atomic layers increased up to five by increasing the volume of the precursor solution from 12.0 to 16.0 and 22.0 mL, respectively. Specifically, the samples shown in Figure 3 correspond to Pd@Pt$_{2\text{–}3\mathrm{L}}$, Pd@Pt$_{3\text{–}4\mathrm{L}}$, and Pd@Pt$_{4\text{–}5\mathrm{L}}$ octahedra. We determined the average number (*n*) of Pt atomic layers for the Pd@Pt$_{n\mathrm{L}}$ octahedra using inductively coupled plasma mass spectrometry (ICP-MS). As shown in Table S4, the average numbers of Pt atomic layers were 2.2, 3.4, and 4.3, respectively, for these three samples. The TEM images indicate that all the samples of Pd@Pt$_{n\mathrm{L}}$ (n=2−5) octahedra were covered by smooth surfaces due to the uniform, conformal deposition of Pt atoms.

Figure 4, A−E, shows high-angle annular dark-field scanning TEM (HAADF-STEM) images of the Pd@Pt$_{2\text{–}3\mathrm{L}}$ octahedra, confirming that the Pt atoms were uniformly deposited on the surfaces of the Pd seeds. In particular, Figure 4B shows that the truncated corners of the Pd seeds were largely preserved during the deposition of Pt. Interestingly, more atomic layers of Pt were deposited at the corner sites than on the side faces. This difference indicates that the Pt atoms preferred to be deposited onto the {100} facets at the corner sites relative to the {111} facets on the side faces, which could be attributed to the difference in surface free energy or atom coordination number.[34] We could observe some surface defects such as steps and vacancy sites on the surface of the Pt shell. Such defects are typically associated with crystal growth in a solution phase *via* a layer-by-layer mechanism,[39] as well as thin film deposition in a gas phase.[40] The observation of such surface defects also supports our claim that the Pt shell was formed in a layer-by-layer fashion due to the slow injection of the Pt precursor and the involvement of a relatively high temperature. Figure 4F shows energy dispersive X-ray (EDX) line scan profiles along the red arrow marked in Figure 4E, further confirming the core-shell structure observed in the STEM images. We also characterized the $Pd@Pt_{3-4L}$ and $Pd@Pt_{4-5L}$ octahedra by STEM and representative images can be found in Figure S4 in the Supporting Information. In general, it is hard to measure the exact number of Pt overlayers on a Pd octahedron due to the complication of orientation (which is different from a cubic system). These STEM images still offer some useful information to support the core-shell structure claimed for these bimetallic nanocrystals.

Electrocatalytic measurements of the $Pd@Pt_{n\mathrm{L}}$ octahedra synthesized in polyol. Prior to the electrochemical measurements, the $Pd@Pt_{n\mathrm{L}}$ octahedra were dispersed onto carbon to obtain $Pd@Pt_{n\mathrm{L}}/C$ catalysts (Figure S5, C−E). The catalysts were then treated with acetic acid at 60 ^{o}C for 2 h to remove residual PVP or bromide ions possibly adsorbed on the surface (Figure S6). Figure 5A shows cyclic voltammograms (CVs) of the catalysts obtained at room temperature in a N_2-saturated aqueous $HClO_4$ solution (0.1 M). Table 1 shows ECSAs of the catalysts derived from the charges associated with the desorption peaks of the underpotentially deposited hydrogen. It is worth noting that the ESCAs of the $Pd@Pt_{n\mathrm{L}}/C$ were comparable or even higher than that of the Pt/C although their particles were much greater in term of size (21 nm *vs.* 3.2 nm). This result implies that the Pt atoms in the $Pd@Pt_{n\mathrm{L}}$ octahedra were better dispersed on the surface than those in the 3.2 nm particles of Pt/C when they were deposited as ultrathin shells of only a few atomic layers thick.

We then measured the ORR current densities of the $Pd@Pt_{n\mathrm{L}}/C$ and Pt/C catalysts at room temperature in an O_2-saturated aqueous $HClO_4$ solution (0.1 M) with a rotation speed of 1,600 rpm for the working electrode (Figure 5B). From each polarization curve, we calculated the kinetic current density (j_k) for ORR using the Koutecky-Levich equation and then normalized it to the ECSA for specific activity ($j_{\mathrm{k,specific}}$, Figure 5C) and to the Pt mass for the mass activity ($j_{\mathrm{k,mass}}$, Figure 5D). To quantitatively understand their performance for ORR, we took the values of both specific and mass activities at 0.9 V_{RHE} and plotted them in Figure 5, E and F, relative to those of Pt/C. All the Pd@Pt$_{n\mathrm{L}}$/C catalysts exhibited around four-fold enhancement in specific activity relative to the Pt/C (Table 1). Such an enhancement in specific activity could be attributed to a combination of the enlargement in proportion for the {111} facets on the surface and the electronic coupling between Pd and Pt. As shown by DFT calculations and experimental measurements, Pt(111) is more active than Pt(100) toward ORR. While the small Pt particles in the Pt/C catalyst were likely enclosed by a mix of {100}, {111}, and {211} facets, the Pd@Pt$_{n\mathrm{L}}$ octahedra were mainly enclosed by {111} facets in addition to the minor presence of {100} facets at the corner sites. As indicated by DFT calculations, the Pd core could weaken the binding of OH on the surface of the catalyst by modulating the electronic structure of the Pt shell, leading to acceleration of the ORR kinetics. The mass activities of the Pd@Pt$_{2-3\mathrm{L}}$/C, Pd@Pt$_{3-4\mathrm{L}}$/C, and Pd@Pt$_{4-5\mathrm{L}}$/C based upon mass of Pt were 0.48, 0.40, and 0.34 A $\mathrm{mg}_{\mathrm{Pt}}^{-1}$, respectively, which were 5.4, 4.5, and 3.8 times higher than that of the Pt/C catalyst (Table 1). The significant improvement in mass activity for the Pd@Pt$_{n\mathrm{L}}$/C catalysts could be attributed to the enhancement in both specific ORR activity and dispersion of Pt atoms. While the mass activities of the Pd@Pt$_{n\mathrm{L}}$/C in terms of Pt decreased with increasing the number (n) of Pt overlayers, the mass activities in terms of precious metals (*i.e.*, both Pt and Pd) did not change significantly (Figure 5F).

In addition to the assessment of catalytic activity, we carried out an accelerated durability test to evaluate the long-term stability of the Pd@Pt$_{n\mathrm{L}}$/C catalysts. The test was conducted by applying a linear potential sweep between 0.6 and 1.1 V_{RHE} at a rate of 0.1 V s^{-1} in an O_2-saturated aqueous $HClO_4$ solution (0.1 M) at room temperature. The Pd@Pt$_{n\mathrm{L}}$/C catalysts exhibited significantly improved durability compared to the commercial Pt/C. At 0.9 V_{RHE}, the mass activity of Pd@Pt$_{2-3\mathrm{L}}$/C, Pd@Pt$_{3-4\mathrm{L}}$/C, and Pd@Pt$_{4-5\mathrm{L}}$/C only dropped by 28.9%, 8.7% and 17.6%, respectively, after 10,000 cycles, while the mass activity of the Pt/C dropped by 54% after only 5,000 cycles (Figure 5G). As shown in Figure 5H, the changes to ORR mass activity during the durability test corresponded well to the variations in specific surface area. The ECSAs of Pd@Pt$_{2-3\mathrm{L}}$/C, Pd@Pt$_{3-4\mathrm{L}}$/C, and Pd@Pt$_{4-5\mathrm{L}}$/C were reduced by 36.0%, 12.3%, and 12.8% after 10,000 cycles. In the case of the Pt/C, its rapidly diminished ECSA could be attributed to the loss of the Pt nanoparticles during repeated cycles of ORR. Previous studies have demonstrated that the small nanoparticles in the Pt/C could be easily dissolved under harsh conditions such as repeated ORR cycles in an O_2-saturated solution.[27] Agglomeration among the Pt nanoparticles could also contribute to the decrease in ECSA for the Pt/C catalyst. In contrast to the very small particles in the Pt/C, the Pd@Pt_{nL} octahedra could be better protected from dissolution and/or agglomeration during the durability test because of their relatively large size. The Pd core could also inhibit the corrosion of the Pt shell by sacrificing itself, resulting in the enhancement in durability for ORR.

Synthesis of Pd@Pt_{nL} octahedra using the water-based protocol. For the water-based synthesis, we only focused on Pd@$Pt_{2–3L}$ octahedra because they were anticipated to exhibit the highest mass activity toward ORR among all the samples with *n* varying between two and five. To establish the optimal protocol for the synthesis of Pd@$Pt_{2–3L}$ octahedra in a water-based system, we conducted a systematic study by changing the experimental parameters one by one from the standard procedure for the polyol-based protocol. Figure 6 shows a series of TEM images for the products obtained during the optimization of protocol. First, we carried out the synthesis by using the standard procedure for the polyol-based protocol except for the drop in reaction temperature from 200 to 95 ^{o}C (Figure 6A). We then conducted the reaction in water instead of EG at 95 ^{o}C (Figure 6B). For both samples, the particle surfaces were not as smooth as those for the Pd@$Pt_{2–3L}$ octahedra obtained using the standard procedure at 200 ^{o}C (Figure 3B). Due to the reduction in temperature, the Pt adatoms on the Pd octahedra could not diffuse to spread across the entire surfaces to generate overlayers with smooth surfaces. In addition, the Pt(IV) precursor could not be completely reduced to Pt atoms due to the weakened reducing power of EG and AA at a low temperature and thus the Pt content (*wt*%) in the product dropped from 29.1 (Figure 3A) to 13.0 (Figure 6A) and 10.7 (Figure 6B).

To deposit more Pt atoms on the seeds, we added more Pt(IV) precursor (from 2.1 to 31.3 μmol of Na_2PtCl_6) into the reaction solution (Figure 6C). In this case, self-nucleated Pt particles were found to coexist with the core-shell octahedra and the Pt content was still at low level of 11.5 *wt*%. This result implies that small Pt particles were formed through self-nucleation due to the increase in concentration for the newly formed Pt atoms in the reaction solution, but most of these small Pt particles were lost during centrifugation and washing. To avoid self-nucleation, we switched to a mild reducing agent such as CA in an effort to maintain the Pt atoms at a very low concentration in the reaction solution (Figure 6D).[17,41,42] Using this protocol, we obtained nanoparticles with a hollow structure, which is believed to result from the galvanic replacement reaction between $Pt(IV)Cl_6^{2-}$ and Pd octahedral seeds. To prevent the galvanic replacement reaction, we switched the precursor from $Pt(IV)Cl_6^{2-}$ to $Pt(II)Cl_4^{2-}$. However, the product still suffered from the galvanic replacement reaction (Figure 6E). It has been reported that the galvanic replacement reaction between $Pt(II)Cl_4^{2-}$ and Pd could be accelerated in presence of Br^- ions in the reaction solution.[17,43] When we removed KBr from the reaction solution, we successfully obtained solid nanocrystals with smooth surfaces (Figure 6F). We then added the precursor solution rapidly in one-shot in lieu of injecting dropwise (Figure 7A). If we can introduce the precursor solution in one-shot to synthesize the $Pd@Pt_{nL}$ octahedra, the protocol can be easily extended to the continuous droplet reactor for large scale production.[38]

Figure 7A shows a TEM image of the $Pd@Pt_{2-3L}$ octahedra, representing the uniform deposition of Pt on the Pd seeds as evidenced by their smooth surfaces. Although we rapidly added the K_2PtCl_4 solution into the reaction solution in one-shot, we could obtain only the $Pd@Pt_{2-3L}$ octahedra without small Pt nanoparticles. It represents that the use of mild reducing agent, CA, could resulted in very low concentration of the free Pt atoms in the reaction solution suppressing the self-nucleation. In particular, different from the $Pd@Pt_{nL}$ octahedra from the polyol-based system, the product particles have sharp corners. This indicates that the decreased reaction temperature in the water-based protocol slowed down the diffusion of the Pt adatoms from the corners to side faces. The HAADF-STEM images in Figure 7, B−E clearly reveal the formation of a conformal shell of Pt epitaxially grown on the Pd(111) surface. The Pt atoms were evenly deposited on all the side faces of a Pd octahedron, with an average Pt shell thickness of 2−3 atomic layers. The average number of the Pt layers was further confirmed as 2−3 by calculating the Pt and Pd contents obtained from ICP-MS analysis (Table S4). An EDX line scan in Figure 7F indicates that the Pt shell was formed on the surface of the Pd core with a thickness around 0.6 nm, which corresponds to the STEM images.

To understand the possible impact of solvent on the synthesis of $Pd@Pt_{2-3L}$ octahedra, we have also conducted additional syntheses by employing the standard procedure for the water-based protocol, except for the use of EG or diethylene glycol (DEG) as a solvent. As shown in Figure S7, small Pt nanoparticles were formed due to self-nucleation. Different from water, this result indicates that both EG and DEG have reducing power toward K_2PtCl_4. To eliminate self-nucleation, the precursor has to be used at a lower concentration (see Figure 6) and introduced dropwise if EG or DEG is used as the solvent. As such, it is difficult to directly compare the products prepared using different solvents because experimental conditions other than the solvent also need to be altered in order to avoid self-nucleation.

Electrocatalytic measurements of the Pd@Pt$_{n\mathrm{L}}$ octahedra synthesized in water. We also measured the electrocatalytic properties of the Pd@Pt$_{2\text{–}3\mathrm{L}}$ octahedra obtained using the water-based protocol. After obtaining the CV (Figure 8A), we estimated the ECSA of the Pd@Pt$_{2\text{–}3\mathrm{L}}$/C catalyst and the value was found to be slightly higher than that of the Pt/C (Table 1). However, the value was not as high as that of the Pd@Pt$_{2\text{–}3\mathrm{L}}$/C prepared using the polyol-based protocol, which could be attributed to the increased amount of Pt atoms at the corner sites when the synthesis was conducted in water at a much lower temperature. From the polarization curve in Figure 8B, we calculated the kinetic current density (j_k) for ORR using the Koutecky-Levich equation and then normalized it to the ECSA and Pt mass to obtain the specific activity ($j_\mathrm{k,specific}$) and mass activity ($j_\mathrm{k,mass}$), respectively (Figure 8, C and D). The specific and mass activities at 0.9 V_RHE based upon the Pt mass are plotted in Figure 8, E and F, showing that the Pd@Pt$_{2\text{–}3\mathrm{L}}$/C exhibited five-fold enhancement relative to the commercial Pt/C, for both the specific and mass activities (Table 1). Interestingly, the specific activity of the Pd@Pt$_{2\text{–}3\mathrm{L}}$/C catalyst prepared in a water-based system exhibited was higher compared to that of its counterpart obtained from the polyol-based system (0.91 mA $\mathrm{cm_{Pt}^{-2}}$ *vs.* 0.73 mA $\mathrm{cm_{Pt}^{-2}}$). This difference can be attributed to the fact that the nanocrystals synthesized in water were enclosed by well-defined {111} surfaces while those obtained in polyol were enclosed by a mix of {111} and {100} facets due to truncation at the corner sites.

We further conducted an accelerated durability test for the Pd@Pt$_{2\text{–}3\mathrm{L}}$/C catalyst synthesized *via* the water-based route. Like the catalysts prepared using the polyol-based protocol, the catalyst also showed remarkably improved durability relative to the Pt/C. The mass activity of the Pd@Pt$_{2\text{–}3\mathrm{L}}$/C catalyst (water-based) only dropped by 13% and 46% after 10,000 and 20,000 cycles, respectively, while the mass activity of the Pt/C dropped by 54% after only 5,000 cycles (Figure 5G). The ECSA of the catalyst showed changes similar to the ORR mass activity during the durability test (Figure 5H). The TEM images taken from the Pd@Pt$_{2\text{–}3\mathrm{L}}$/C sample after the accelerated durability test suggest that the Pd cores were sacrificed during the repeated cycles of ORR due to its higher reactivity than Pt (Figure S8). In practice, this strategy could be used to prevent the dissolution of Pt and thus improve the durability of a Pt-based ORR catalyst.

CONCLUSION

We have demonstrated the syntheses of Pd@Pt$_{n\mathrm{L}}$ (n=2−5) core-shell octahedra through the conformal, epitaxial deposition of Pt on Pd octahedral seeds using two different protocols based upon polyol and water, respectively. For the polyol-based system, the slow injection of a Pt(IV) precursor, the accelerated surface diffusion of Pt adatoms at a relatively high temperature, and the small mismatch in lattice constant between Pd and Pt all played important roles in enabling the layer-by-layer overgrowth. Significantly, the number (n) of Pt atomic layer could be tuned from two to five by simply introducing more precursor into the growth solution. Significantly, we were able to extend the concept of atomic layer-by-layer deposition from a polyol- to a water-based system and, at the same time, significantly reduce the reaction temperature from 200 ^{o}C to 95 ^{o}C. Furthermore, we could introduce all the precursor in one-shot by slowing down the reduction of a Pt(II) compound with the use of a mild reducing agent. All of the Pd@Pt$_{n\mathrm{L}}$ octahedra exhibited at least four folds enhancement in specific activity toward ORR when compared to a commercial Pt/C based upon 3.2-nm Pt particles. Our DFT calculations suggested that this enhancement could be attributed to the destabilization of OH on the surfaces of the Pd@Pt$_{n\mathrm{L}}$ octahedra with respect to the Pt/C. This destabilization facilitates OH hydrogenation, the rate-limiting step for ORR. As a result of the enhancement in specific activity and the increase in dispersion for the Pt atoms, the Pd@Pt$_{n\mathrm{L}}$ octahedra also showed significant enhancement in mass activity when compared to the commercial Pt/C. Due to the involvement of particles with much enlarged sizes, the catalysts based upon Pd@Pt$_{n\mathrm{L}}$ octahedra exhibited remarkably improved durability, making them a potential replacement for the commercial ORR catalyst based upon Pt/C.

EXPERIMENTAL SECTION

Materials. All the chemicals were used as received from Sigma-Aldrich (unless specified). These include sodium tetrachloropalladate(II) (Na_2PdCl_4, 98%), sodium hexachloroplatinate(IV) hexahydrate ($Na_2PtCl_6 \cdot 6H_2O$, 98%), potassium tetrachloroplatinate(II) (K_2PtCl_4, 99.99%), poly(vinyl pyrrolidone) (PVP, MW≈55,000), formaldehyde (Fisher Scientific), ascorbic acid (AA, 99%), citric acid (CA, 99.5%), potassium bromide (KBr, 99%), ethylene glycol (EG, 99%, J. T. Baker), and ethanol (200 proof, KOPTEC). All aqueous solutions were prepared using deionized (DI) water with a resistivity of 18.2 MΩ cm.

Synthesis of Pd cubes and octahedra. The Pd nanocubes (6 and 10 nm in edge length)[44] and Pd octahedra (15 and 19 nm in edge length)[45] were synthesized, respectively, using protocols recently reported by our group. For the synthesis of Pd octahedra, a suspension of the Pd cubes (0.3 mL, 2.0 mg mL^{-1}), and formaldehyde (0.1 mL) were added into an aqueous solution (8 mL) containing PVP (105 mg) and the mixture was heated at 60 ^{o}C for 10 min under magnetic stirring. An aqueous solution (3 mL) containing Na_2PdCl_4 (29 mg) was then quickly added into the preheated solution. The reaction solution was kept at 60 ^{o}C for 3 h under magnetic stirring. The reaction solution was cooled down to room temperature. The product was collected by centrifugation, washed twice with DI water, and re-dispersed in EG (2 mL) or DI water (10 mL). The Pd octahedra of 15 and 19 nm in edge length were synthesized from the Pd cubes of 6 and 10 nm in edge length, respectively.

Synthesis of Pd@Pt$_{n\mathrm{L}}$ octahedra in the polyol-based system. For the synthesis of Pd@Pt$_{n\mathrm{L}}$ octahedra in polyol, 1 mL of the Pd octahedra suspension (19 nm in edge length, 1.12 mg mL^{-1}), 67 mg PVP, 100 mg AA, 54 mg KBr, and 12 mL EG were mixed in a three-neck flask and heated at 110 ^{o}C for 1 h under magnetic stirring. The temperature was then quickly ramped to 200 ^{o}C within 20 min and a specific amount of EG solution containing $Na_2PtCl_6 \cdot 6H_2O$ (0.1 mg mL^{-1}) was added dropwise with a syringe pump at a rate of 4.0 mL h^{-1}. After complete injection, the reaction solution was kept at 200 ^{o}C for 1 h under magnetic stirring and then cooled down to room temperature. The product was collected by centrifugation, washed twice with ethanol and three times with DI water, and re-dispersed in DI water.

Synthesis of Pd@Pt$_{2\text{–}3\mathrm{L}}$ octahedra in the water-based system. For the synthesis of Pd@Pt$_{2\text{–}3\mathrm{L}}$ octahedra in water, 35 mg PVP and 60 mg CA were added into 10 mL of the aqueous suspension of Pd octahedra (15 nm, 0.19 mg mL^{-1}) and then heated at 95 ^{o}C for 10 min under magnetic stirring. Meanwhile, 13 mg K_2PtCl_4 was dissolved in 3 mL of DI water and the solution was quickly added into the pre-heated solution using a pipette. The reaction solution was kept at 95 ^{o}C for 24 h under magnetic stirring and then cooled down to room temperature. The product was collected by centrifugation, washed three times with DI water, and re-dispersed in DI water.

Preparation of carbon-supported Pd@Pt$_{n\mathrm{L}}$ octahedra catalysts (Pd@Pt$_{n\mathrm{L}}$/C). The Pd@Pt$_{n\mathrm{L}}$ octahedra were collected by centrifugation and re-dispersed in 20 mL of ethanol. A specific amount of carbon black (Ketjenblack EC-300J, AkzoNobel) was added into the suspension to obtain a loading of about 20 *wt*% for both Pt and Pd. The mixture was then ultrasonicated for 3 h and the resulting Pd@Pt$_{n\mathrm{L}}$/C was collected by centrifugation, re-dispersed in 10 mL of acetic acid, and heated at 60 ^{o}C for 2 h to remove PVP or bromide on the surface of the particles. The Pd@Pt$_{n\mathrm{L}}$/C catalyst was washed three times with ethanol and dried in an oven at 70 ^{o}C for 30 min prior to the use for ORR tests.

Morphological, structural, and elemental analysis. Transmission electron microscopy (TEM) was done with an HT7700 microscope (Hitachi) operated at 120 kV. High-angle annular dark-field scanning TEM (HAADF-STEM) and energy dispersive X-ray (EDX) scanning analyses were performed using an ARM200F microscope (JEOL) with STEM aberration corrector operated at 200 kV. Inductively coupled plasma mass spectrometry (ICP-MS, NexION 300Q, Perkin-Elmer) was used for a quantitative analysis of metal contents in the sample.

Electrochemical characterizations. Electrochemical measurements were performed using a glassy carbon rotating disk electrode (RDE, Pine Research Instrumentation) connected to a potentiostat (CHI 600E, CH Instruments). An ink for the electrochemical measurement was prepared by adding 3 mg of the Pd@Pt$_{n\mathrm{L}}$/C into a mixture of DI water (1 mL), isopropanol (1 mL, Sigma-Aldrich), and Nafion (5% solution, Sigma-Aldrich, 40 μL), followed by sonication for 10 min. A working electrode was prepared by loading the ink (20 μL) on the glassy carbon electrode. Another working electrode was prepared from the carbon-supported Pt catalyst (Pt/C, 20 *wt*% 3.2 nm nanoparticles on Vulcan XC-72 carbon support, Premetek) using the same protocol. An Ag/AgCl electrode (BASi) and a Pt mesh were used as the reference and counter electrodes, respectively. The potentials (V_{RHE}) were converted to values with reference to the reversible hydrogen electrode (RHE). The electrolyte was an aqueous $HClO_4$ solution (Baker) with a concentration of 0.1 M.

The cyclic voltammograms (CVs) were measured in a N_2-saturated electrolyte by cycling between 0.05 and 1.1 V_{RHE} at a sweep rate of 0.05 V s^{-1}. To calculate the ECSA, we measured the charges (Q_H) generated from the desorption of hydrogen between 0.05 and 0.4 V_{RHE} with a reference value of 210 μC cm^{-2} for the desorption of a monolayer of hydrogen from a Pt surface and then divided by the mass of Pt loaded on the working electrode. The ORR test was carried out in an O_2-saturated electrolyte with a scan rate of 0.01 V s^{-1} and a rotation speed of 1,600 rpm. The kinetic current density (j_k) was derived from the Koutecky-Levich equation as follows:

$$\frac{1}{j} = \frac{1}{j_k} + \frac{1}{j_d}$$

where j is measured current density and j_d is the diffusion-limiting current density.

For the accelerated durability tests, the CVs and ORR polarization curves were measured after sweeping 5,000, 10,000, and 20,000 cycles between 0.6 and 1.1 V_{RHE} at a rate of 0.1 V s^{-1} in an O_2-saturated aqueous $HClO_4$ solution at room temperature.

Conflict of Interest: The authors declare no competing financial interest.

Supporting Information Available: Detailed method for DFT calculations; thermodynamic stability of Pt_{1L}*/Pd(111) with different compositions for the top layer; TEM images and size distribution of the Pd octahedral seeds; TEM images of the products obtained through the protocol for Pd@Pt_{nL} cubes with Pd octahedral seeds; HAADF-STEM images of Pd@Pt_{3-4L} and Pd@Pt_{4-5L} octahedra; TEM images of Pt/C and Pd@Pt_{nL}/C catalysts; XPS spectra of the Pd@Pt_{2-3L} octahera; TEM images of the products obtained through the standard procedures of the water-based protocol in EG and DEG; TEM images of Pd@Pt_{2-3L}/C after the durability test; a table of free energies for the hydrogenation of O and OH on the model surfaces; a table of the binding energies for O and OH on the model surfaces; a table showing centers of d_{z^2}-bands of model surfaces; a table of the number (n) of Pt atomic layers of Pd@Pt_{nL} octaehdra. This material is available free of charge *via* the Internet at http://pubs.acs.org.

Acknowledgment. The syntheses were supported by startup funds from the Georgia Institute of Technology while the calculations were supported by DOE-BES (Office of Chemical Sciences, grant DE-FG02-05ER15731). As a visiting graduate student from Xiamen University, L.Z. was also partially supported by a fellowship from the China Scholarship Council. The calculations were performed using the facilities at supercomputing centers located at EMSL (sponsored by the DOE Office of Biological and Environmental Research at PNNL); CNM at ANL (supported by DOE contract DE-AC02-06CH11357); and NERSC (supported by DOE contract DE-AC02-05CH11231).

REFERENCES AND NOTES

1. Gasteiger, H. A.; Kocha, S. S.; Sompalli, B.; Wagner, F. T. Activity benchmarks and requirements for Pt, Pt-alloy, and non-Pt oxygen reduction catalysts for PEMFCs. *Appl. Catal., B* **2005**, *56*, 9−35.
2. Vielstich, W.; Lamm, A.; Gasteiger, H. A. *Handbook of Fuel Cells−Fundamentals, Technology and Applications*; John Wiley & Sons: Chichester, 2003.
3. Shao, M. *Electrocatalysis in Fuel Cells: A Non- and Low-Platinum Approach*; Springer: London, 2013.
4. Steele, B. C. H.; Heinzel, A. Materials for fuel-cell technologies. *Nature* **2001**, *414*, 345−352.
5. Perry, M. L.; Fuller, T. F. J. A Historical Perspective of Fuel Cell Technology in the 20th Century. *Electrochem. Soc.* **2002**, *149*, S59−S67.
6. Chen, J.; Lim, B.; Lee, E. P., Xia, Y. Shape-controlled synthesis of platinum nanocrystals for catalytic and electrocatalytic applications. *Nano Today* **2009**, *4*, 81−95.
7. Department of Energy. *Multi-Year Research, Development and Demonstration Plan*, http://www.eere.energy.gov, 2012.
8. Tian, N.; Zhou, Z.-Y.; Sun, S.-G.; Ding, Y.; Wang, Z. L. Synthesis of Tetrahexahedral Platinum Nanocrystals with High-Index Facets and High Electro-Oxidation Activity. *Science* **2007**, *316*, 732−735.
9. Bratlie, K. M.; Lee, H.; Komvopoulos, K.; Yang, P.; Somorjai, G. A. Platinum Nanoparticle Shape Effects on Benzene Hydrogenation Selectivity. *Nano Lett.* **2007**, *7*, 3097−3101.
10. Wang, C.; Daimon, H.; Onodera, T.; Koda, T.; Sun, S. A General Approach to the Size- and Shape-Controlled Synthesis of Platinum Nanoparticles and Their Catalytic Reduction of Oxygen. *Angew. Chem. Int. Ed.* **2008**, *47*, 3588−3591.

11. Chen, C.; Kang, Y.; Huo, Z.; Zhu, Z.; Huang, W.; Xin, H. L.; Snyder, J. D.; Li, D.; Herron, J. A.; Mavrikakis, M.; Chi, M.; More, K. L.; Li, Y.; Marković, N. M.; Somorjai, G. A.; Yang, P.; Stamenkovic, V. R. Highly Crystalline Multimetallic Nanoframes with Three-Dimensional Electrocatalytic Surfaces. *Science* **2014**, *343*, 1339−1343.
12. Zhang, H.; Jin, M.; Xia, Y. Enhancing the catalytic and electrocatalytic properties of Pt-based catalysts by forming bimetallic nanocrystals with Pd. *Chem. Soc. Rev.* **2012**, *41*, 8035−8049.
13. Stamenkovic, V. R.; Mun, B. S.; Arenz, M.; Mayrhofer, K. J. J.; Lucas, C. A.; Wang, G.; Ross, P. N.; Marković, N. M. Trends in electrocatalysis on extended and nanoscale Pt-bimetallic alloy surfaces. *Nat. Mater.* **2007**, *6*, 241−247.
14. Choi, S.-I.; Xie, S.; Shao, M.; Odell, J. H.; Lu, N.; Peng, H.-C.; Protsailo, L.; Guerrero, S.; Park, J.; Xia, X.; Wang, J.; Kim, M. J.; Xia, Y. Synthesis and Characterization of 9 nm Pt–Ni Octahedra with a Record High Activity of 3.3 A/mg$_{Pt}$ for the Oxygen Reduction Reaction. *Nano Lett.* **2013**, *13*, 3420−3425.
15. Choi, S.-I.; Xie, S.; Shao, M.; Lu, N.; Guerrero, S.; Odell, J. H.; Park, J.; Wang, J.; Kim, M. J.; Xia, Y. Controlling the Size and Composition of Nanosized Pt–Ni Octahedra to Optimize Their Catalytic Activities toward the Oxygen Reduction Reaction. *ChemSusChem* **2014**, *7*, 1476−1483.
16. Lim, B.; Jiang, M.; Camargo, P. H. C.; Cho, E. C.; Tao, J.; Lu, X.; Zhu, Y.; Xia, Y. Pd-Pt Bimetallic Nanodendrites with High Activity for Oxygen Reduction. *Science* **2009**, *5*, 1302−1305.
17. Zhang, H.; Jin, M.; Wang, J.; Kim, M. J.; Yang, D.; Xia, Y. Nanocrystals Composed of Alternating Shells of Pd and Pt Can Be Obtained by Sequentially Adding Different Precursors. *J. Am. Chem. Soc.* **2011**, *133*, 10422−10425.
18. Zhang, J. L.; Vukmirovic, M. B.; Xu, Y.; Mavrikakis, M.; Adzic, R. R. Controlling the Catalytic Activity of Platinum-Monolayer Electrocatalysts for Oxygen Reduction with Different Substrates. *Angew. Chem. Int. Ed.* **2005**, *44*, 2132−2135.
19. Vukmirovic, M. B.; Zhang, J.; Sasaki, K.; Nilekar, A. U.; Uribe, F.; Mavrikakis, M.; Adzic, R. R. Platinum monolayer electrocatalysts for oxygen reduction. *Electrochim. Acta* **2007**, *52*, 2257−2263.
20. Liu, Y.; Gokcen, D.; Bertocci, U.; Moffat, T. P. Self-Terminating Growth of Platinum Films

by Electrochemical Deposition. *Science* **2012**, *338*, 1327−1330.

21. Kitchin, J. R.; Nørskov, J. K.; Barteau, M. A.; Chen, J. G. Role of Strain and Ligand Effects in the Modification of the Electronic and Chemical Properties of Bimetallic Surfaces. *Phys. Rev. Lett.* **2004**, *93*, 156801-1−156801-4.
22. Wang, J. X.; Inada, H.; Wu, L.; Zhu, Y.; Choi, Y.; Liu, P.; Zhou, W.-P.; Adzic, R. R. J. Oxygen Reduction on Well-Defined Core−Shell Nanocatalysts: Particle Size, Facet, and Pt Shell Thickness Effects. *J. Am. Chem. Soc.* **2009**, *131*, 17298−17302.
23. Wang, X.; Orikasa, Y.; Takesue, Y.; Inoue, H.; Nakamura, M.; Minato, T.; Hoshi, N.; Uchimoto, Y. Quantitating the Lattice Strain Dependence of Monolayer Pt Shell Activity toward Oxygen Reduction. *J. Am. Chem. Soc.* **2013**, *135*, 5938−5941.
24. Strasser, P.; Koh, S.; Anniyev, T.; Greeley, J.; More, K.; Yu, C.; Liu, Z.; Kaya, S.; Nordlund, D.; Ogasawara, H.; Toney, M. F.; Nilsson, A. Lattice-strain control of the activity in dealloyed core–shell fuel cell catalysts. *Nat. Chem.* **2010**, *2*, 454−460.
25. Greeley, J.; Mavrikakis, M. Alloy catalysts designed from first principles. *Nat. Mater.* **2004**, *3*, 810−815.
26. Alayoglu, S.; Nilekar, A. U.; Mavrikakis, M.; Eichhorn, B. Ru–Pt core–shell nanoparticles for preferential oxidation of carbon monoxide in hydrogen. *Nat. Mater.* **2008**, *7*, 333−338.
27. Xie, S.; Choi, S.-I.; Lu, N.; Roling, L. T.; Herron, J. A.; Zhang, L.; Park, J.; Wang, J.; Kim, M. J.; Xie, Z.; Mavrikakis, M.; Xia, Y. Atomic Layer-by-Layer Deposition of Pt on Pd Nanocubes for Catalysts with Enhanced Activity and Durability toward Oxygen Reduction. *Nano. Lett.* **2014**, *14*, 3570−3576.
28. Stamenkovic, V. R.; Fowler, B.; Mun, M. S.; Wang, G. F.; Ross, P. N.; Lucas, C. A.; Marković, N. M. Improved Oxygen Reduction Activity on $Pt_3Ni(111)$ via Increased Surface Site Availability. *Science* **2007**, *315*, 493−497.
29. Zhang, J.; Yang, H.; Fang, J.; Zou, S. Synthesis and Oxygen Reduction Activity of Shape-Controlled Pt_3Ni Nanopolyhedra. *Nano Lett.* **2010**, *10*, 638−644.
30. Zhou, W.; Wu, J.; Yang, H. Highly Uniform Platinum Icosahedra Made by Hot Injection-Assisted GRAILS Method. *Nano Lett.* **2013**, *13*, 2870−2874.
31. Adzic, R. R., Zhang, J.; Sasaki, K.; Vukmirovic, M. B.; Shao, M.; Wang, J. X.; Nilekar, A. U.; Mavrikakis, M.; Valerio, J. A.; Uribe, F. Platinum Monolayer Fuel Cell Electrocatalysts. *Top. Catal.* **2007**, *46*, 249−262.

32. Shao, M.; He, G.; Peles, A.; Odell, J. H.; Zeng, J.; Su, D.; Tao, J.; Yu, T.; Zhu, Y.; Xia, Y. Manipulating the oxygen reduction activity of platinum shells with shape-controlled palladium nanocrystal cores. *Chem. Commun.* **2013**, *49*, 9030−9032.
33. Xia, X.; Xie, S.; Liu, M.; Peng, H.-C.; Lu, N.; Wang, J.; Kim, M. J.; Xia, Y. On the role of surface diffusion in determining the shape or morphology of noble-metal nanocrystals. *P. Natl. Acad. Sci. U. S. A.* **2013**, *110*, 6669−6673.
34. Xia, Y.; Xiong, Y.; Lim, B.; Skrabalak, S. E. Shape-Controlled Synthesis of Metal Nanocrystals: Simple Chemistry Meets Complex Physics? *Angew. Chem. Int. Ed.* **2009**, *48*, 60−103.
35. Lim, B.; Jiang, M.; Tao, J.; Camargo, P. H. C.; Zhu, Y.; Xia, Y. Shape-Controlled Synthesis of Pd Nanocrystals in Aqueous Solutions. *Adv. Funct. Mater.* **2009**, *19*, 189−200.
36. Nørskov, J. K.; Rossmeisl, J.; Logadottir, A.; Lindqvist, L. Origin of the Overpotential for Oxygen Reduction at a Fuel-Cell Cathode. *J. Phys. Chem. B* **2004**, *108*, 17886−17892.
37. Koper, M. T. M. Thermodynamic theory of multi-electron transfer reactions: Implications for electrocatalysis. *J. Electroanal. Chem.* **2011**, *660*, 254−260.
38. Zhang, Lei; Xia, Y. Scaling up the Production of Colloidal Nanocrystals: Should We Increase or Decrease the Reaction Volume? *Adv. Mater.* **2014**, *26*, 2600–2606.
39. Lim, B.; Kobayashi, H.; Camargo, P. H. C.; Allard, L. F.; Liu, J.; Xia, Y. New Insights into the Growth Mechanism and Surface Structure of Palladium Nanocrystals. *Nano Res.* **2010**, *3*, 180−188.
40. Zhang, Z.; Lagally, M. G. Atomistic Processes in the Early Stages of Thin-Film Growth. *Science* **1997**, *276*, 377−383.
41. Lim, B.; Wang, J.; Camargo, P. H. C.; Jiang, M.; Kim, M.; Xia, Y. Facile Synthesis of Bimetallic Nanoplates Consisting of Pd Cores and Pt Shells through Seeded Epitaxial Growth. *Nano Lett.* **2008**, *8*, 2535−2540.
42. Jiang, M.; Lim, B.; Tao, J.; Camargo, P. H. C.; Ma, C.; Zhu, Y.; Xia, Y. Epitaxial overgrowth of platinum on palladium nanocrystals. *Nanoscale* **2010**, *2,* 2406−2411.
43. Zhang, H.; Jin, M.; Wang, J.; Li, W.; Camargo, P. H. C.; Kim, M. J.; Yang, D.; Xie, Z.; Xia, Y. Synthesis of Pd-Pt Bimetallic Nanocrystals with a Concave Structure through a Bromide-Induced Galvanic Replacement Reaction. *J. Am. Chem. Soc.* **2011**, *133*, 6078−6089.
44. Jin, M.; Liu, H.; Zhang, H.; Xie, Z.; Liu, J.; Xia, Y. Synthesis of Pd nanocrystals enclosed by

{100} facets and with sizes <10 nm for application in CO oxidation. *Nano Res.* **2011**, *4*, 83−91.

45. Jin, M.; Zhang, H.; Xie, Z.; Xia, Y. Palladium nanocrystals enclosed by {100} and {111} facets in controlled proportions and their catalytic activities for formic acid oxidation. *Energy Environ. Sci.* **2012**, *5*, 6352−6357.

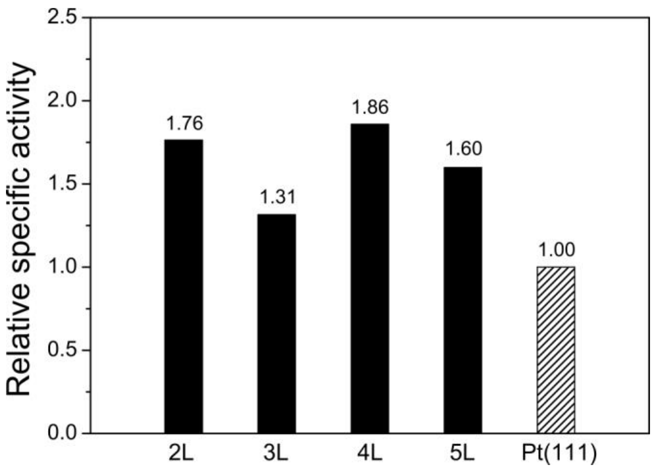

Figure 1. Relative specific activities of Pd@Pt_{nL} (n=2−5) octahedra at 0.9 V_{RHE} that were calculated using Pt_{nL}*/Pd(111) model slabs by DFT. All values are presented relative to Pt(111). All the catalysts based upon Pd@Pt_{nL} (n=2−5) octahedra are anticipated to exhibit improved specific activity relative to Pt octahedra, which are represented by Pt(111).

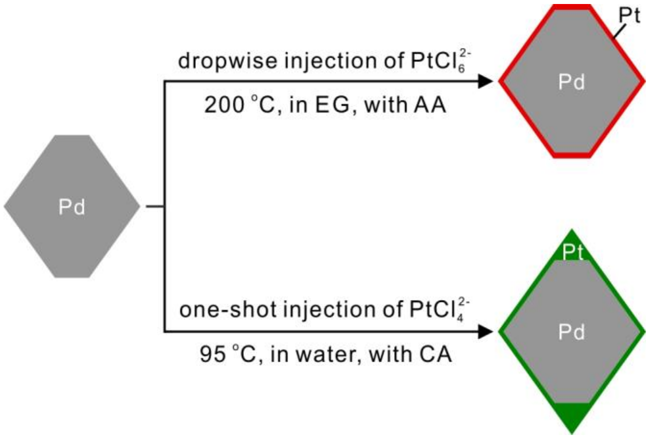

Figure 2. A schematic diagram showing the syntheses of Pd@Pt$_{n\mathrm{L}}$ octahedra *via* two different routes involving polyol and water, respectively. For the synthesis in polyol, a Na_2PtCl_6 solution in ethylene glycol (EG) is titrated dropwise into the reaction solution at 200 °C. Due to the use of a relatively high temperature, the core-shell octahedra show truncation at the corners, just like the original Pd seeds. For the synthesis in water, an aqueous solution of K_2PtCl_4 is added in one-shot into the reaction solution at 95 °C. The use of a much lower reaction temperature results in the formation of Pd@Pt$_{n\mathrm{L}}$ octahedra with sharper corners than the products of a polyol synthesis.

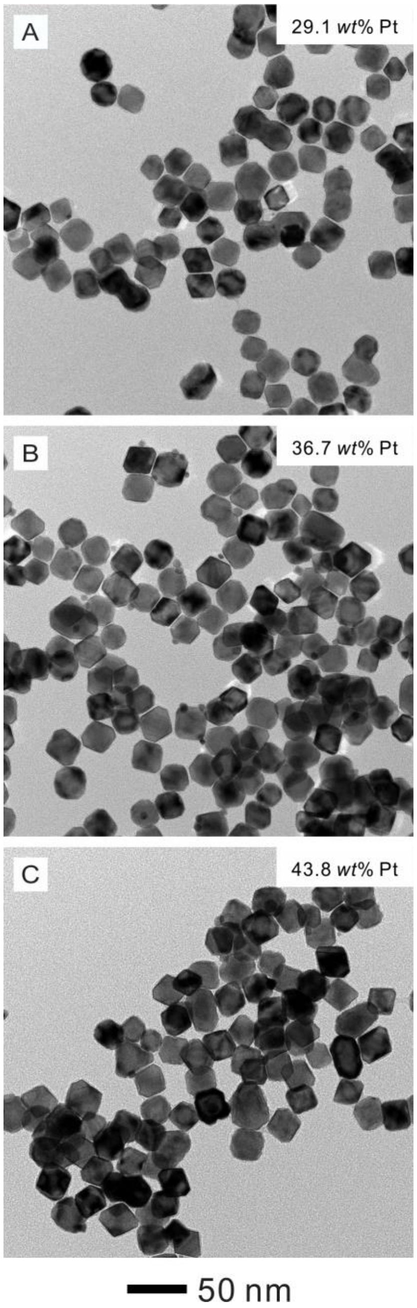

Figure 3. TEM images of Pd@Pt$_{n\mathrm{L}}$ octahedra synthesized using the polyol-based protocol: (A) Pd@Pt$_{2\text{–}3\mathrm{L}}$, (B) Pd@Pt$_{3\text{–}4\mathrm{L}}$, and (C) Pd@Pt$_{4\text{–}5\mathrm{L}}$ octahedra. The volumes of the Na_2PtCl_6 solution (0.10 mg mL^{-1}) added into the reaction solution were 12.0, 16.0, and 22.0 mL, respectively. The number (*n*) of Pt atomic layers was derived from the ICP-MS data. For each sample, the Pt content (*wt*%) from ICP-MS analysis is shown in the inset.

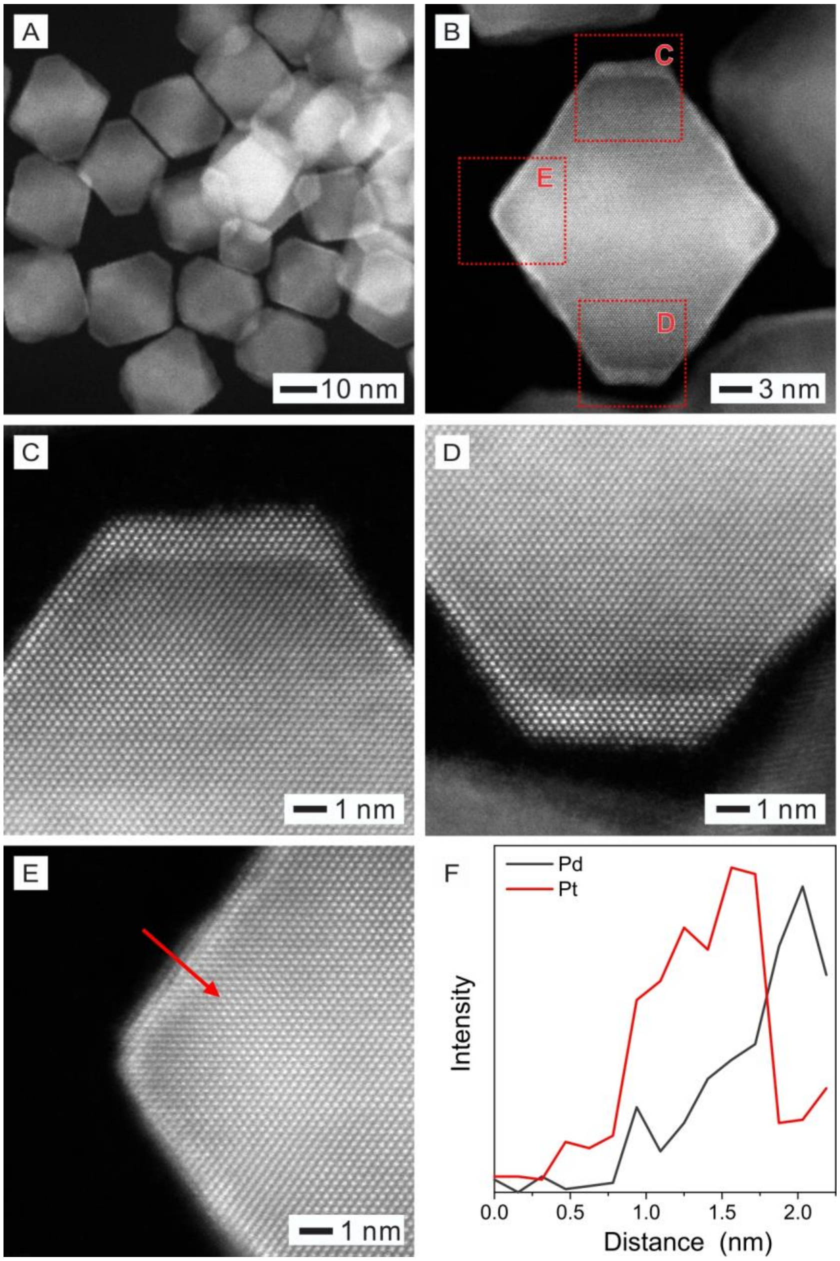

Figure 4. (A−E) HAADF-STEM images of the Pd@Pt$_{2-3L}$ octahedra synthesized using the polyol-based protocol. In the STEM images, the dark and bright regions correspond to Pd and Pt, respectively. (F) EDX line scanning profiles of Pd and Pt for the Pd@Pt$_{2-3L}$ octahedron along the red arrow marked in (E).

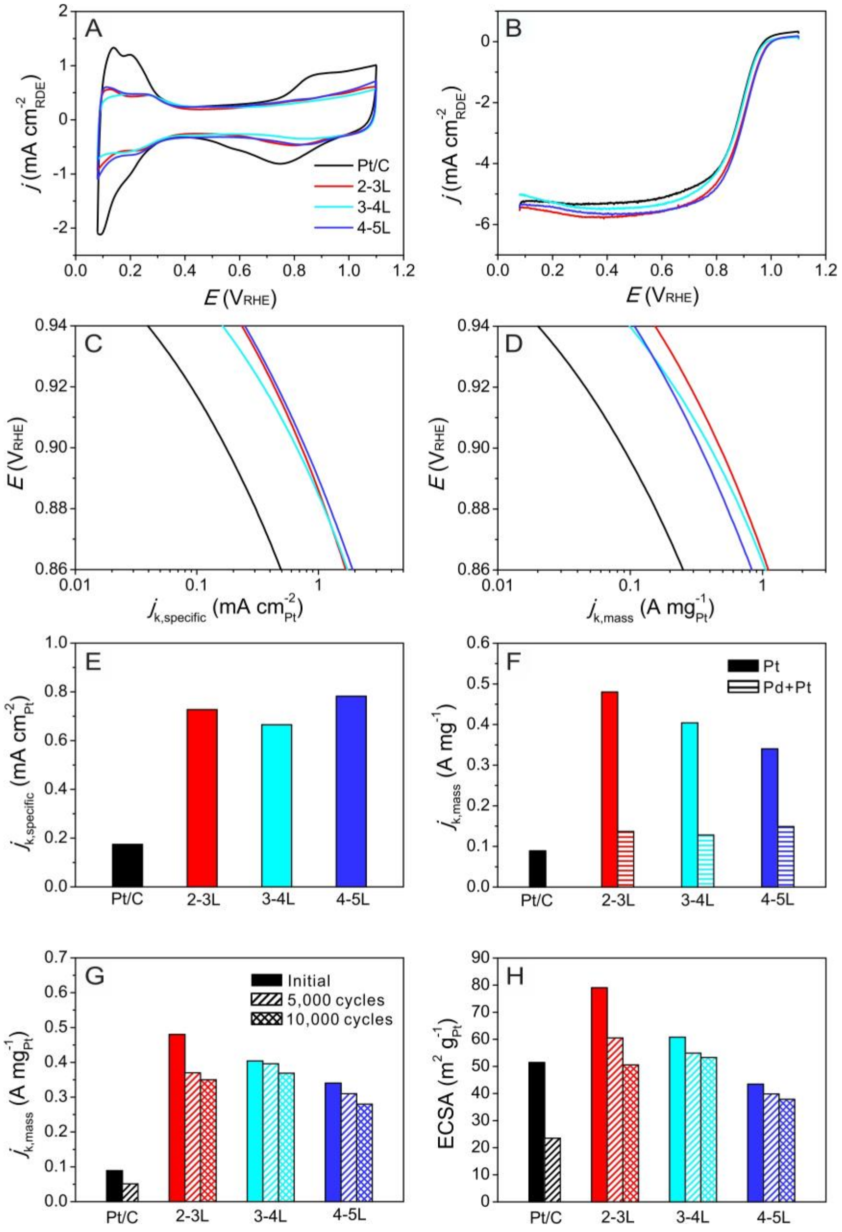

Figure 5. (A) CVs and (B) ORR polarization curves for the Pd@Pt$_{n\text{L}}$/C and commercial Pt/C catalysts. The Pd@Pt$_{n\text{L}}$ octahedra were synthesized using the standard, polyol-based protocol. The current densities (j) were normalized against the geometric area of RDE (0.196 cm^2). (C) Specific and (D) mass activities given as kinetic current densities (j_k) normalized against the ECSA of the catalyst and the mass of Pt, respectively. (E) Specific and (F) mass activities (normalized against the masses of Pt and Pd+Pt, respectively) at 0.9 V$_{RHE}$ for the catalysts. (G) Mass activities (at 0.9 V$_{RHE}$) and (H) ECSAs of the catalysts before and after the accelerated durability tests.

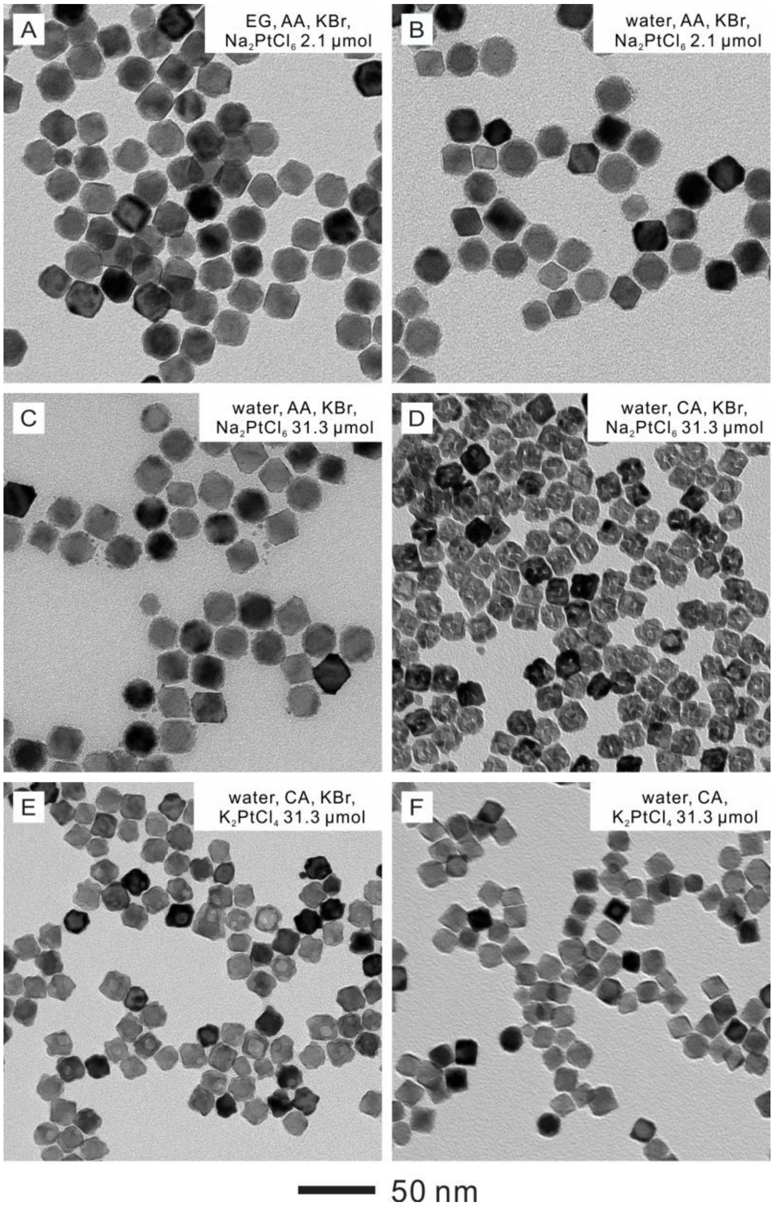

Figure 6. TEM images of the products obtained under various conditions where the experimental parameters were changed one-by-one from the standard protocol for the polyol-based system to the water-based system: (A) the standard procedure for the polyol-based synthesis of Pd@Pt$_{2–3L}$ octahedra except for the reduction of temperature from 200 to 95 ^{o}C; (B) the procedure used for the synthesis in (A) except for the use of water as a solvent; (C) the procedure for the synthesis in (B) except for the increase of Na_2PtCl_6 to 31.3 μmol; (D) the procedure for the synthesis in (C) except for the change of reducing agent from AA to CA; (E) the procedure for the synthesis in (D) except for the use of K_2PtCl_4 for a precursor; and (F) the procedure for the synthesis in (E) except for the absence of KBr.

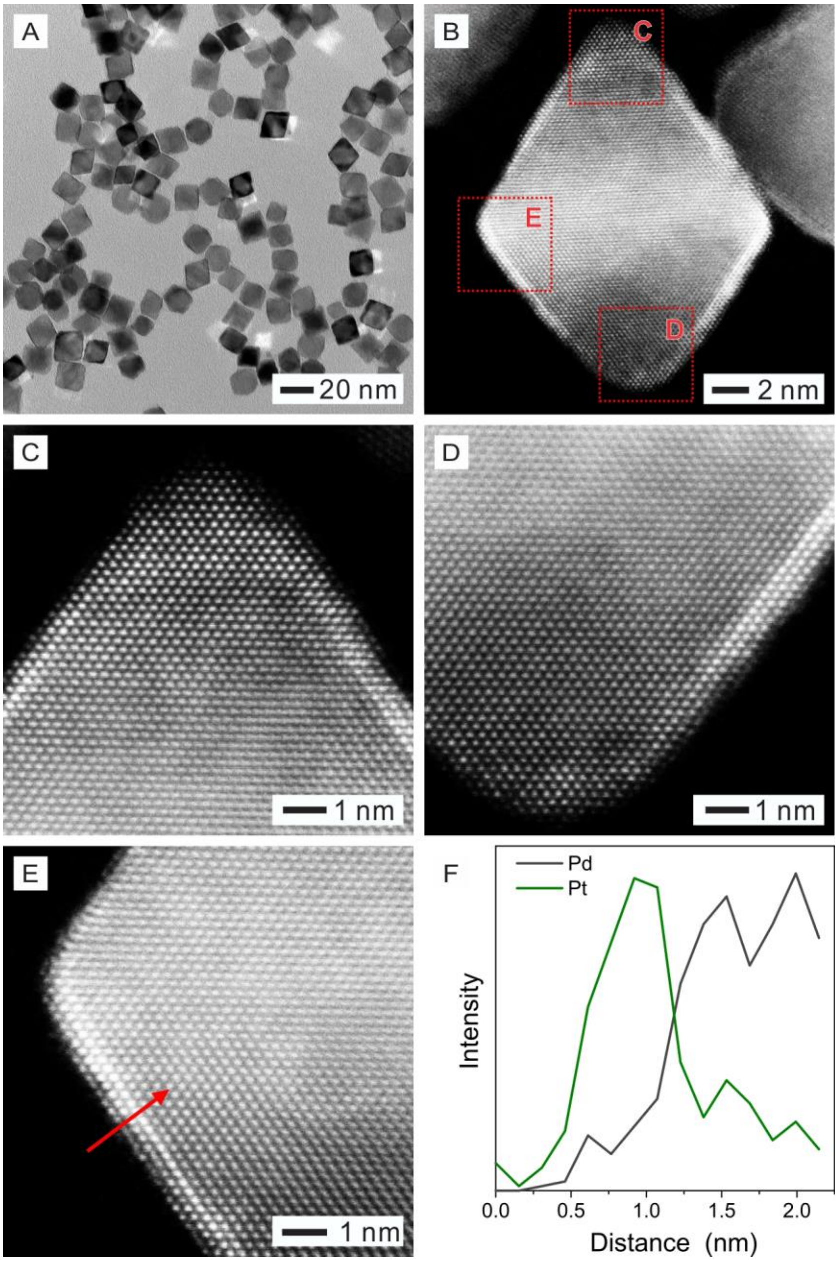

Figure 7. (A) TEM and (B−E) HAADF-STEM images of the Pd@Pt$_{2-3L}$ octahedra synthesized using the standard protocol based upon water. In the STEM images, the dark and bright regions correspond to Pd and Pt, respectively. (F) EDX line scanning profiles of Pd and Pt for the Pd@Pt$_{2-3L}$ octahedron along the red arrow marked in (E).

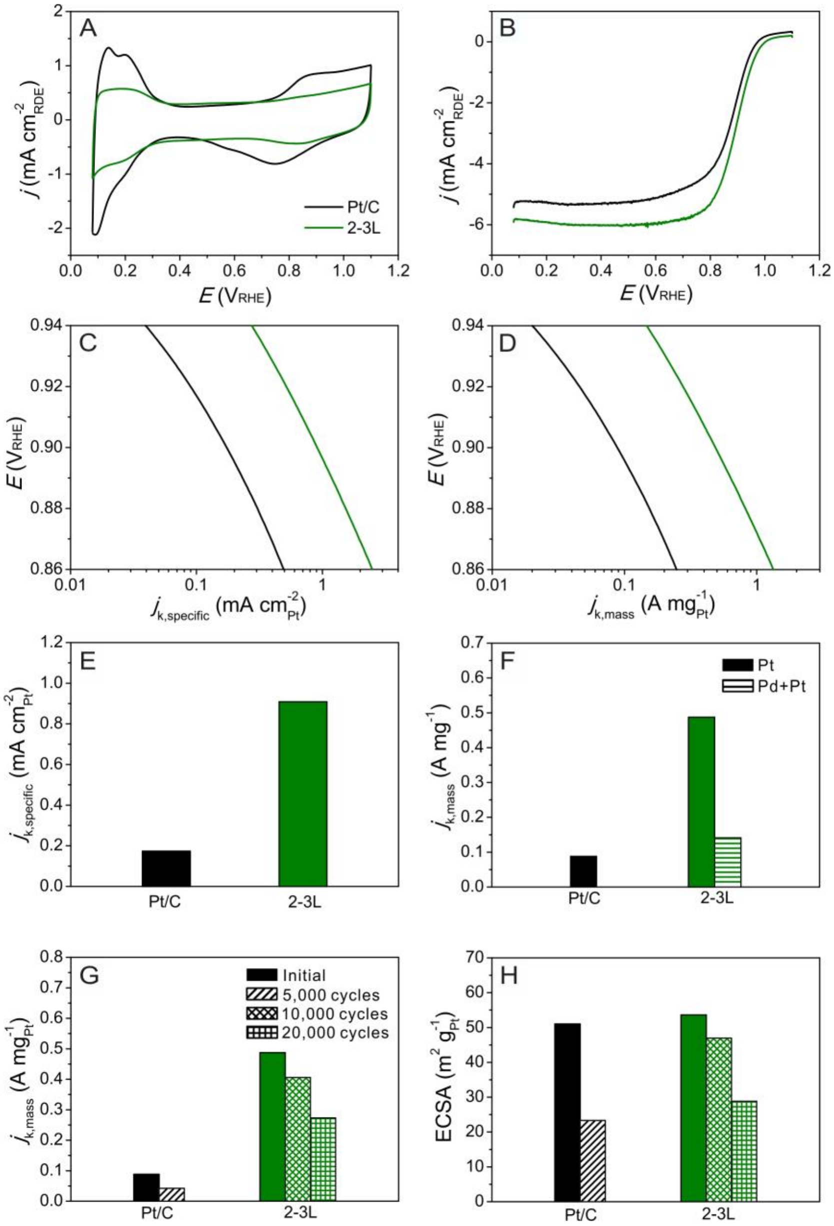

Figure 8. (A) CVs and (B) ORR polarization curves for the Pd@Pt$_{2–3L}$/C and commercial Pt/C catalysts. The Pd@Pt$_{2–3L}$ octahedra were synthesized using the standard, water-based protocol. The current densities (*j*) were normalized against the geometric area of the RDE (0.196 cm^2). (C) Specific and (D) mass activities given as kinetic current densities (j_k) normalized against the ECSA of the catalyst and the mass of Pt, respectively. (E) Specific and (F) mass activities (normalized against the masses of Pt and Pd+Pt, respectively) at 0.9 V$_{RHE}$ for the catalysts. (G) Mass activities (0.9 V$_{RHE}$) and (H) ECSAs of the catalysts before and after the accelerated durability tests.

Table 1. Comparison of the electrochemical surface area (ECSA), specific activity (SA), and mass activity (MA) for the ORR catalysts based upon Pt/C and Pd@Pt$_{n\text{L}}$/C.

Catalyst	ECSA (m^2 g_{Pt}^{-1})	SA at 0.9 V_{RHE} (mA cm_{Pt}^{-2})	MA at 0.9 V_{RHE} (A mg_{Pt}^{-1})	Synthesis method
Pt/C	51.0	0.17	0.089	-
Pd@Pt$_{2–3\text{L}}$/C	79.0	0.73	0.48	Polyol-based system
Pd@Pt$_{3–4\text{L}}$/C	60.8	0.67	0.40	
Pd@Pt$_{4–5\text{L}}$/C	43.4	0.78	0.34	
Pd@Pt$_{2–3\text{L}}$/C	53.6	0.91	0.49	Water-based system

Supporting Information

Atomic Layer-by-Layer Deposition of Pt on Pd Octahedra for Enhanced Catalysts toward the Oxygen Reduction Reaction

Jinho Park,[†,#] Lei Zhang,[‡,#] Sang-Il Choi,[‡] Luke T. Roling,[§] Ning Lu,[∥] Jeffrey A. Herron,[§] Shuifen Xie,[‡] Jinguo Wang,[∥] Moon J. Kim,[∥] Manos Mavrikakis,[§] and Younan Xia*,[†,‡]

[†]School of Chemistry and Biochemistry, Georgia Institute of Technology, Atlanta, Georgia 30332, Unites States

[‡]The Wallace H. Coulter Department of Biomedical Engineering, Georgia Institute of Technology and Emory University, Atlanta, Georgia 30332, Unites States

[§]Department of Chemical and Biological Engineering, University of Wisconsin-Madison, Madison, Wisconsin 53706, United States

[∥]Department of Materials Science and Engineering, University of Texas at Dallas, Richardson, Texas 75080, United States

[#]These two authors contributed equally to this work.

*Corresponding author: younan.xia@bme.gatech.edu

DFT Calculations

Calculations were performed using plane wave density functional theory (DFT), as implemented in the Dacapo code.[1,2] The exchange-correlation potential and energy were described self-consistently by the GGA-PW91 functional.[3,4] The ionic cores were described by ultrasoft Vanderbilt pseudopotentials.[5] Due to the relatively small differences in measured ORR activities, the surface Brillouin zone was sampled with a 10x10x1 Monkhorst-Pack *k*-point mesh,[6] and the Kohn-Sham one-electron valence states were expanded on the basis of plane waves with a kinetic energy cutoff of 400 eV; these criteria are tighter than would typically be used for this type of calculation. Eighteen special Chadi-Cohen *k*-points[7] and a kinetic energy cutoff of 340 eV were used for calculations of diffusion activation energy barriers, which were determined using the climbing image nudged elastic band (CI-NEB) method.[8] The vibrational frequencies of adsorbed intermediates were determined from the diagonalization of the mass-weighted Hessian matrix. A second order finite difference approach, using a step size of 0.015 Å, was used to numerically differentiate the forces.[9] The entropies and zero-point energies (ZPE) of surface species were calculated from the vibrational frequencies using the harmonic oscillator approximation. ZPE and entropic contributions to total energy for adsorption on $\mathrm{Pt}_{n\mathrm{L}}$*/Pd(111) surfaces were assumed to be the same as on Pt(111), due to the similar optimized geometries of each intermediate on those surfaces.

All calculations were performed on slabs with seven metal layers, in which the top five layers were allowed to fully relax. The $\mathrm{Pt}_{n\mathrm{L}}$*/Pd(111) surfaces were modeled by replacing the top *n* layers by Pt atoms (*n*=2−5). These slabs were constructed using the optimized bulk lattice constant of Pd (3.99 Å). A pure Pt(111) slab was also constructed using the optimized bulk lattice constant of Pt (4.00 Å). Both optimized lattice constants are in good agreement with the experimental values (3.89 Å and 3.92 Å for Pd and Pt, respectively).[10] A 2x2 periodic surface unit cell was used, corresponding to a surface coverage of 0.25 monolayers (ML) of each adsorbate.

Surface diffusion of Pt adatoms. The Pd@$\mathrm{Pt}_{n\mathrm{L}}$ octahedra could be synthesized at 95 °C, which is a considerably lower temperature than what was needed for the synthesis of Pd@$\mathrm{Pt}_{n\mathrm{L}}$ nanocubes (200 °C).[11] In general, a sufficiently high temperature is required to accelerate the diffusion of Pt adatoms across the Pd surface, thereby avoiding the formation of Pt islands on the surface. As a first investigation of this phenomenon, we calculated the diffusion barrier of Pt adatoms across a Pd(100) surface (as a model for the cubes) and a Pd(111) surface (as a model for the octahedra). We found that the diffusion of a Pt adatom across Pd(100) has a relatively large activation energy barrier (E_A) of 1.06 eV. In contrast, the diffusion of Pt across Pd(111) has a very small barrier of only 0.16 eV, which corresponds to a rate constant, k ($k \propto \exp\left(-\frac{E_A}{k_B T}\right)$, where k_B is the Boltzmann constant and T is absolute temperature), which is more than 15 orders of magnitude higher at room temperature. A fundamental reason for the difficulty of diffusion across the (100) facet is the stronger binding of adatoms due to its under coordination relative to the (111) facet. The Pt atoms bind to three-fold hollow sites on the Pd(111) surface, while they bind to four-fold hollow sites on the Pd(100) surface. The diffusion barrier of adsorbates across a metal surface has been shown to correlate with the binding energy of adsorbates.[12] In particular, our calculations indicate that Pt binds more strongly to the Pd(100) facet than the Pd(111) by 0.63 eV. Our findings are therefore in agreement with this expectation, and support the experimental observations that higher temperatures are needed to facilitate energetically demanding diffusion on Pd cubic seeds.

ORR activity of surface models. To understand the experimentally observed enhanced activity of the Pd@Pt$_{n\text{L}}$ octahedra relative to Pt/C and the Pd@Pt$_{n\text{L}}$ cubes, we performed self-consistent periodic DFT calculations to determine the binding energies of adsorbed O and OH on model surfaces. The Pd@Pt$_{n\text{L}}$ octahedra were modeled as Pt$_{n\text{L}}$*/Pd(111) extended surfaces (with the lattice constant of Pd), while Pt/C was modeled using Pt(111) and Pt(100) extended surfaces (with the lattice constant of Pt). In our previous work,[11] the Pd@Pt$_{n\text{L}}$ cubes were modeled as Pt$_{n\text{L}}$*/Pd(100) extended surfaces (with nearly identical calculation parameters as in this study). The binding energies (BEs) of adsorbed species were calculated as $BE = E_{\text{total}} - E_{\text{clean slab}} - E_{\text{gas phase}}$, where E_{total} is the total energy of the adsorbate on the slab, $E_{\text{clean slab}}$ is the total energy of the slab without the adsorbate, and $E_{\text{gas phase}}$ is the total energy of the isolated adsorbate in the gas phase.

The free energy changes (ΔG) of elementary steps with proton/electron transfer were calculated as a function of electrode potential using the computational hydrogen electrode developed by Nørskov and coworkers:[13] $\Delta G = \Delta E + \Delta ZPE - T\Delta S + |e|U$, where ΔE is the change in total energy, ΔZPE is the zero-point-energy correction, T is the absolute temperature

(298 K), ΔS is the change in entropy, $|e|$ is the absolute value of charge of an electron, and U is the electrode operating potential. The electrochemical reference was chosen to be the reversible hydrogen electrode (RHE), in which the reaction $H_2 \leftrightarrow 2\,(H^+ + e^-)$ is in equilibrium at a defined potential of 0 V under standard conditions. Therefore, the hydrogenation reactions considered in this study become more *endothermic* as U becomes more positive. When calculating free energies, adsorbed OH was stabilized by 0.5 eV on (111) surface and by 0.1 eV on (100) surface to account for interactions with the water bilayer.[14] The free energies of reaction were tabulated in Table S1. For all surfaces studied, OH hydrogenation is more difficult than O hydrogenation, and therefore is assumed to be the rate-limiting step.

As in our previous work,[11] we performed a simple Sabatier analysis[13] to understand the effect of OH binding on the ORR activity. We calculated the rate constant of OH hydrogenation (the rate-limiting step) with an Arrhenius formula. We set the activation energy of elementary reaction steps equal to the change in free energy of the reaction step, or zero, whichever value is larger. This provides a thermodynamic lower bound for the activation energy of elementary steps.[15] The rate constant of OH hydrogenation on surface i (k_i) was therefore calculated as $k_i = \exp(\frac{-\Delta G_i}{k_\mathrm{B}T})$, where ΔG_i is the free energy change on surface i, k_B is the Boltzmann constant, and T is the absolute temperature (298 K). We calculated the relative activity of each surface by normalizing the rate constants to $k_{Pt(111)}$; therefore, the relative activities shown in Figure 1 of the main text were calculated as $k_i/k_{Pt(111)}$. It is particularly noteworthy that all of the $\mathrm{Pt}_{n\mathrm{L}}$*/Pd(111) ($n$=2−5) surfaces exhibit weaker OH binding than pure Pt(111), suggesting that the Pd@$\mathrm{Pt}_{n\mathrm{L}}$ octahedra would have higher specific activity than pure Pt octahedra.

REFERENCES

1. Hammer, B.; Hansen, L. B.; Nørskov, J. K. Improved adsorption energetics within density-functional theory using revised Perdew-Burke-Ernzerhof functionals. *Phys. Rev. B* **1999**, *59*, 7413−7421.
2. Greeley, J.; Nørskov, J. K.; Mavrikakis, M. Electronic Structure and Catalysis on Metal Surfaces. *Annu. Rev. Phys. Chem.* **2002**, *53*, 319−348.
3. Perdew, J. P.; Chevary, J. A.; Vosko, S. H.; Jackson, K. A.; Pederson, M. R.; Singh, D. J.; Fiolhais, C. Atoms, molecules, solids, and surfaces: Applications of the generalized gradient

approximation for exchange and correlation. *Phys. Rev. B* **1992**, *46*, 6671−6687.

4. White, J. A.; Bird, D. M. Implementation of gradient-corrected exchange-correlation potentials in Car-Parrinello total-energy calculations. *Phys. Rev. B* **1994**, *50*, 4954−4957.
5. Vanderbilt, D. Soft self-consistent pseudopotentials in a generalized eigenvalue formalism. *Phys. Rev. B* **1990**, *41*, 7892−7895.
6. Monkhorst, H. J.; Pack, J. D. Special points for Brillouin-zone integrations. *Phys. Rev. B* **1976**, *13*, 5188−5192.
7. Chadi, D. J.; Cohen, M. L. Special Points in the Brillouin Zone. *Phys. Rev. B* **1973**, *8*, 5747−5753.
8. Henkelman, G.; Uberuaga, B. P.; Jonsson, H. A. A climbing image nudged elastic band method for finding saddle points and minimum energy paths. *J. Chem. Phys.* **2000**, *113*, 9901−9904.
9. Greeley, J.; Mavrikakis, M. A first-principles study of surface and subsurface H on and in Ni(111): diffusional properties and coverage-dependent behavior. *Surf. Sci.* **2003**, *540*, 215−229.
10. Haynes W. M. *CRC Handbook of Chemistry and Physics*; 94th ed.; Taylor and Francis: Boca Raton, 2014.
11. Xie, S.; Choi, S.-I.; Lu, N.; Roling, L. T.; Herron, J. A.; Zhang, L.; Park, J.; Wang, J.; Kim, M. J.; Xie, Z.; Mavrikakis, M.; Xia, Y. Atomic Layer-by-Layer Deposition of Pt on Pd Nanocubes for Catalysts with Enhanced Activity and Durability toward Oxygen Reduction. *Nano. Lett.* **2014**, *14*, 3570−3576.
12. Nilekar, A. U.; Greeley, J.; Mavrikakis, M. A Simple Rule of Thumb for Diffusion on Transition-Metal Surfaces. *Angew. Chem. Int. Ed.* **2006**, *45*, 7046−7049.
13. Nørskov, J. K.; Rossmeisl, J.; Logadottir, A.; Lindqvist, L. Origin of the Overpotential for Oxygen Reduction at a Fuel-Cell Cathode. *J. Phys. Chem. B* **2004**, *108*, 17886−17892.
14. Greeley, J.; Rossmeisl, J.; Hellman, A.; Nørskov, J. K. Theoretical Trends in Particle Size Effects for the Oxygen Reduction Reaction. *Z. Phys. Chem.* **2007**, *221*, 1209−1220.
15. Koper, M. T. M. Thermodynamic theory of multi-electron transfer reactions: Implications for electrocatalysis. *J. Electroanal. Chem.* **2011**, *660*, 254−260.

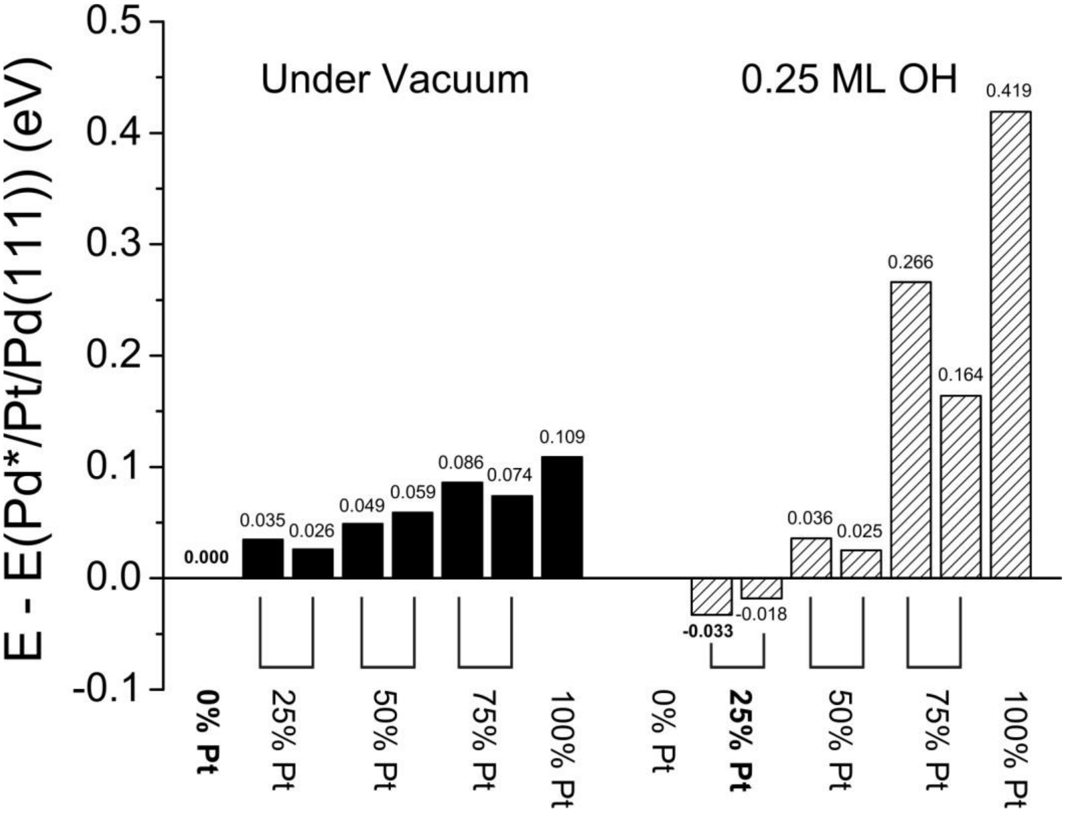

Figure S1. Thermodynamic stability of Pt_{1L}*/Pd(111) calculated under vacuum and in the presence of 0.25 ML OH for the top layer with different compositions. The stability were shown as difference in the total energies between the system with the listed surface composition (% Pt) and the reference state (0% Pt), which is all Pt atoms on the top layer were replaced by Pd atoms of the second layer (Pd*/Pt/Pd(111)). The energy of the Pd-terminated surface is equal to 0 (the reference state). Negative values correspond to more stable configurations while positive values correspond to less stable states. The most stable configuration in each case is indicated using bold letters. Two permutations were considered for 25, 50, and 75% Pt.

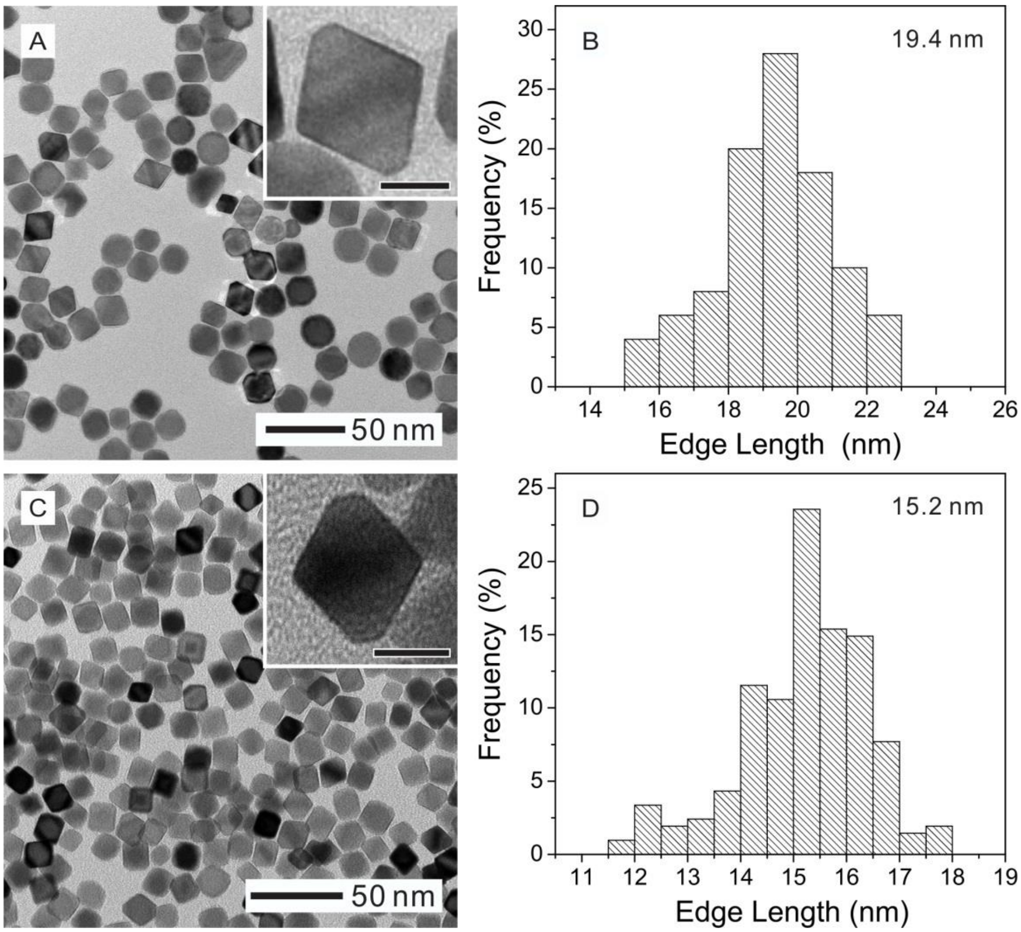

Figure S2. (A, C) TEM images and (B, D) size distributions of the Pd octahedra used as seeds for the synthesis of Pd@Pt$_{n\mathrm{L}}$ octahedra. The insets show TEM images of the Pd octahedron at a higher magnification (scale bar: 10 nm). The Pd octahedra of 19.4 nm and 15.2 nm in average edge length were used for the polyol- and water-based Pt coating protocols, respectively.

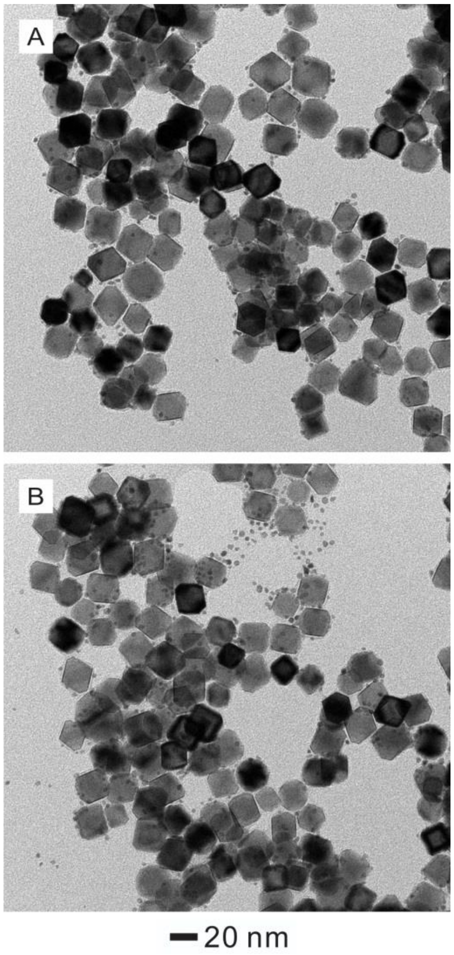

Figure S3. TEM images of the products obtained using the polyol procedure reported for the synthesis of Pd@$\mathrm{Pt}_{2-3\mathrm{L}}$ cubes.[11] In this case, we only replaced the Pd cubic seeds with Pd octahedral seeds with all other parameters kept the same as the standard protocol.

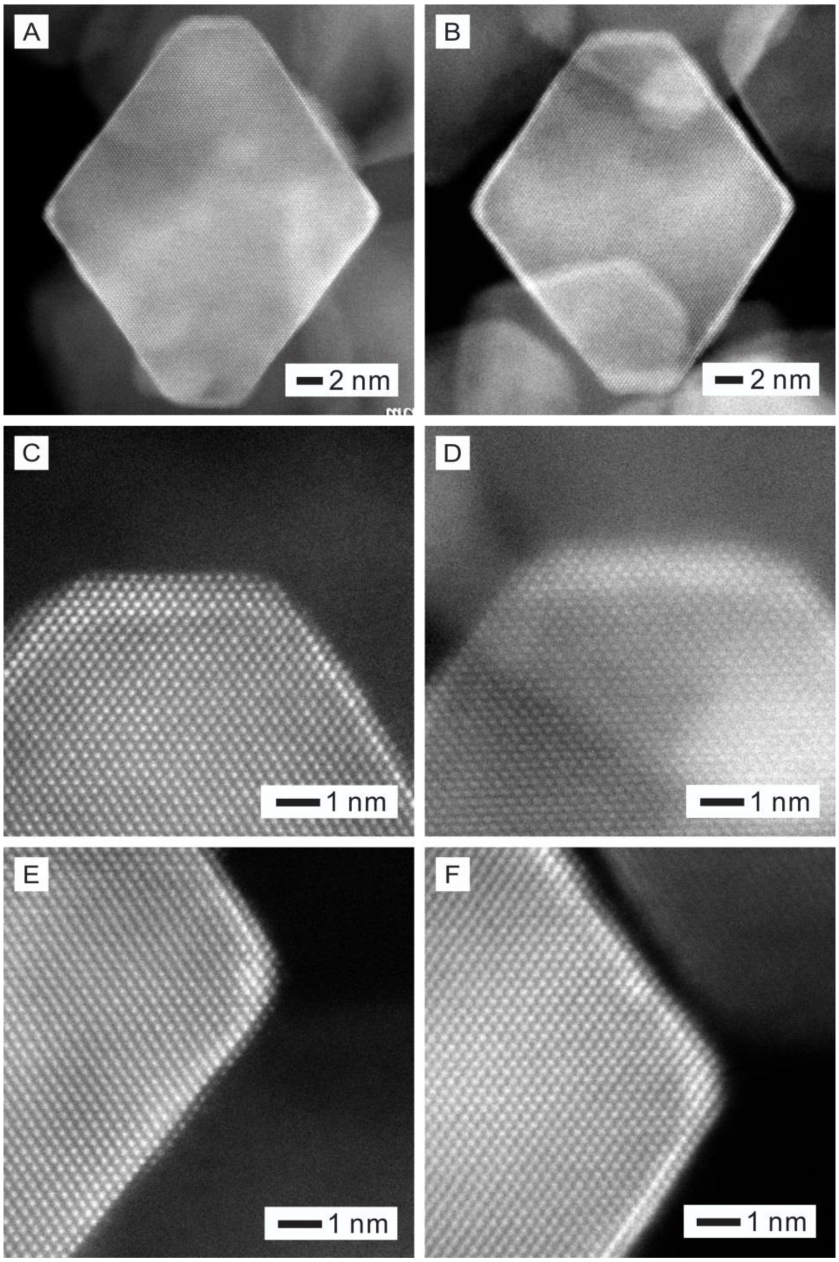

Figure S4. HAADF-STEM images of the Pd@Pt$_{n\mathrm{L}}$ octahedra synthesized using the polyol-based protocol: (A, C, E) Pd@Pt$_{3\text{–}4\mathrm{L}}$ and (B, D, F) Pd@Pt$_{4\text{–}5\mathrm{L}}$ octahedra.

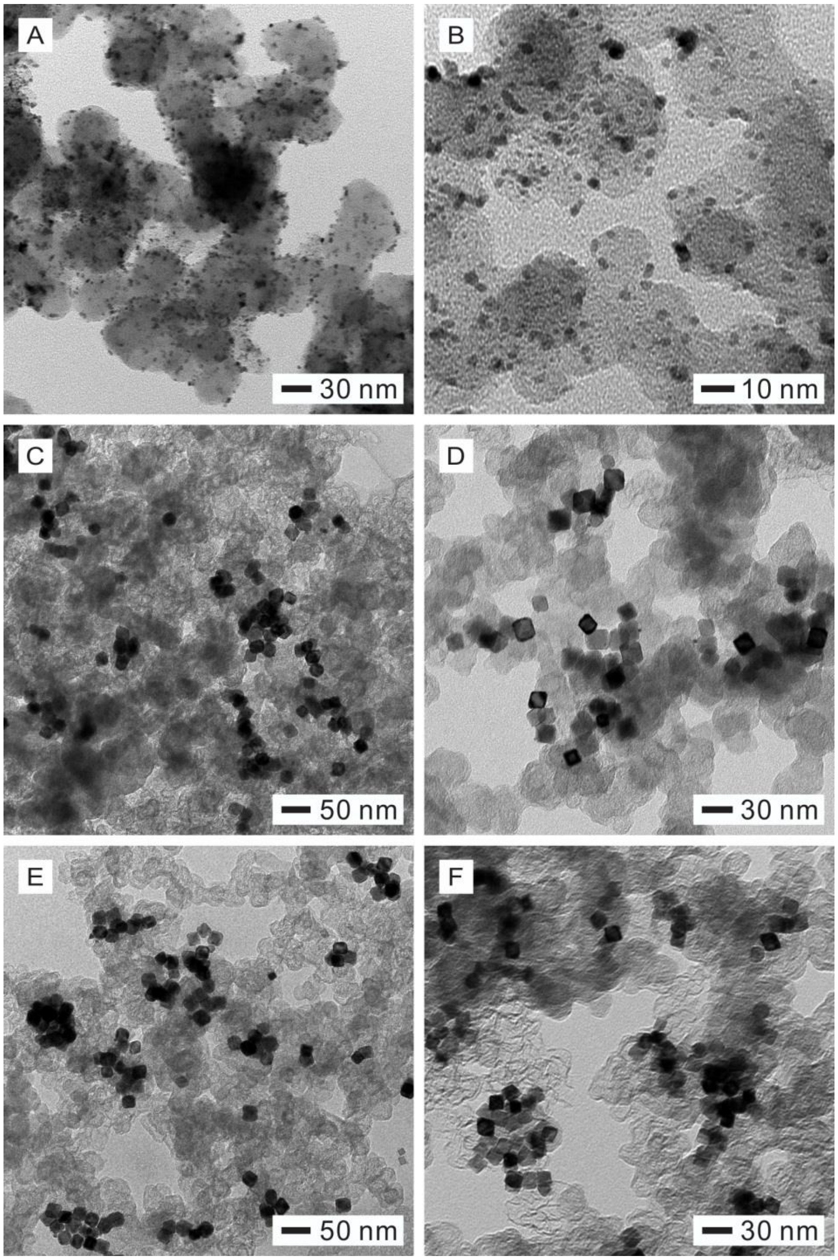

Figure S5. TEM images of the (A, B) Pt/C and (C−F) Pd@Pt$_{n\mathrm{L}}$/C catalysts. The Pd@Pt$_{2\text{–}3\mathrm{L}}$, Pd@Pt$_{3\text{–}4\mathrm{L}}$, and Pd@Pt$_{4\text{–}5\mathrm{L}}$ octahedra shown in (C-E) were synthesized *via* the polyol-based protocol while the Pd@Pt$_{2\text{–}3\mathrm{L}}$ octahedra in (F) were synthesized *via* the water-based protocol.

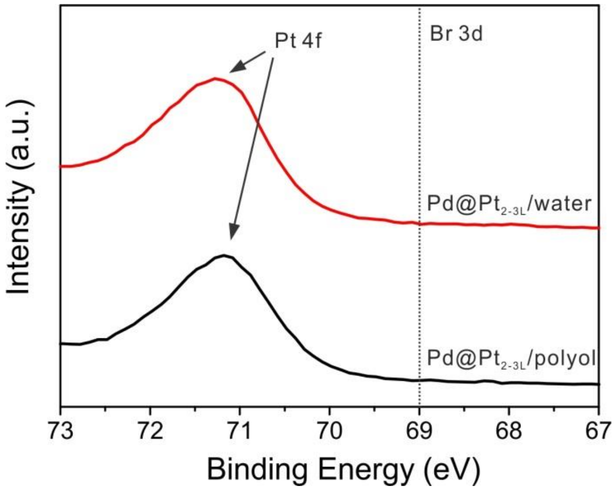

Figure S6. X-ray photoelectron spectra of the Pd@Pt$_{2–3L}$ octahedra prepared using the polyol- (black) and water-based protocols (red), respectively.

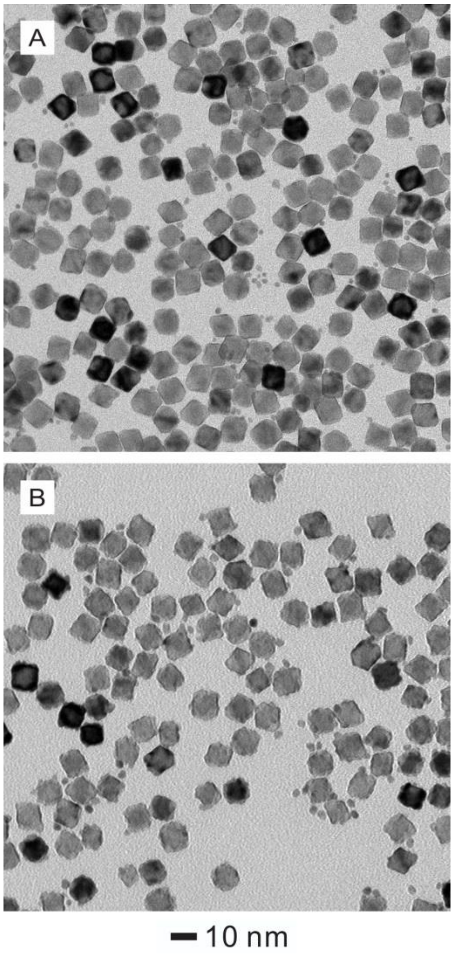

Figure S7. TEM images of the products prepared using the same standard procedure (water-based) as for the synthesis of Pd@Pt$_{2–3L}$ octahedra, except for the use of (A) EG and (B) DEG as the solvents, respectively.

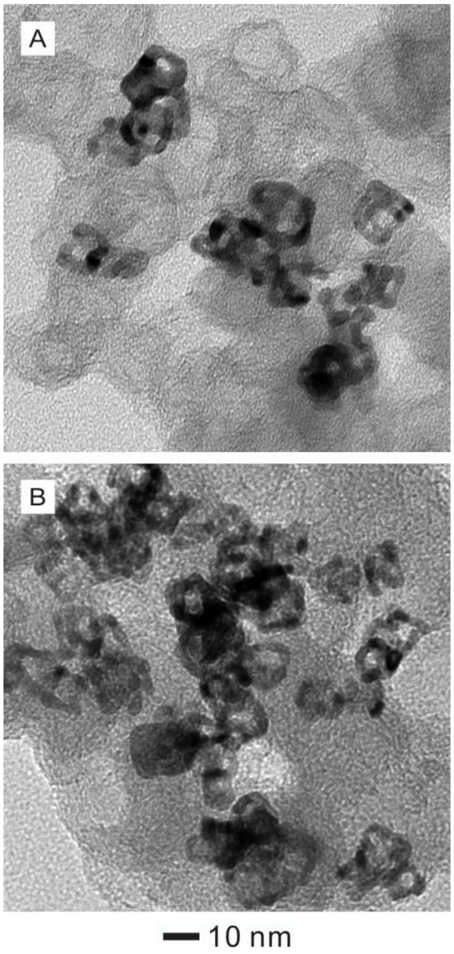

Figure S8. TEM images of the Pd@Pt$_{2-3L}$/C catalyst after the accelerated durability test (20,000 cycles). The Pd@Pt$_{2-3L}$ octahedra were prepared using the water-based protocol.

Table S1. Free energies (Δ*G*) for the hydrogenation of the adsorbed oxygen (O) and hydroxyl (OH) at 0.9 V_{RHE} and 298 K calculated for the model surfaces using DFT.

***n* of Pt atomic layers**	**Δ*G* of the reaction (eV)**			
	Pt_{nL}*/Pd (100)[a]		**Pt_{nL}*/Pd (111)**	
	$O^* + H^+ + e^- \rightarrow OH^*$	**$OH^* + H^+ + e^- \rightarrow H_2O + *$**	**$O^* + H^+ + e^- \rightarrow OH^*$**	**$OH^* + H^+ + e^- \rightarrow H_2O + *$**
2	0.015	0.459	0.125	0.349
3	0.008	0.460	0.117	0.356
4	0.011	0.468	0.114	0.347
5	0.012	0.475	0.110	0.351
Pure Pt	0.015	0.487	0.123	0.363

[a] The values were taken from one of our recent publications,[11] and included here for the purpose of comparison.

Table S2. Binding energies of O and OH on the model surfaces at 0.25 ML coverage derived from DFT calculations.

***n* of Pt atomic layers**	**Binding energy (eV)**			
	Pt_{nL}*/Pd (100)[a]		**Pt_{nL}*/Pd (111)**	
	O	**OH**	**O**	**OH**
2	-3.844	-2.695	-3.867	-2.138
3	-3.838	-2.696	-3.867	-2.145
4	-3.850	-2.705	-3.855	-2.136
5	-3.858	-2.712	-3.855	-2.140
Pure Pt	-3.873	-2.724	-3.879	-2.152
Compressed Pt	-	-	-	-2.144

[a] The values were taken from one of our recent publications,[11] and included here for the purpose of comparison.

Table S3. Center of d_z^2-bands for the model surfaces at 0.25 ML coverage of OH as derived from DFT calculations.

***n* of Pt atomic layers**	**$\varepsilon_{dz2} - \varepsilon_f$ (eV)**
2	-2.480
3	-2.478
4	-2.485

Table S4. The average number (n) of the Pt atomic layers calculated from the Pd and Pt contents in the Pd@Pt$_{n\text{L}}$ octahedra. The metal contents were determined using ICP-MS while the size of the Pd octahedra was derived from TEM.

Sample	**$m_{\text{Pt}}/m_{\text{Pd}}$[a]**	**Thickness of Pt shell (nm)**	**Calculated number of Pt atomic layers**	**number of Pt atomic layers for notation**	**Synthesis method**
Pd@Pt$_{2\text{–}3\text{L}}$	0.41	0.50	2.21	2−3	Polyol-based system
Pd@Pt$_{3\text{–}4\text{L}}$	0.58	0.74	3.36	3−4	
Pd@Pt$_{4\text{–}5\text{L}}$	0.78	0.97	4.29	4−5	
Pd@Pt$_{2\text{–}3\text{L}}$	0.41	0.56	2.47	2−3	Water-based system

[a] The mass ratios of Pt to Pd for the Pd@Pt$_{n\text{L}}$ octahedra were obtained from ICP-MS analysis.